Supplementary Information

Regulating Electron Transfer and Orbital Interaction within Metalloporphyrin-MOF for Highly Sensitive NO_2 Sensing

Er-Xia Chen,[ab] Liang He,[a] Mei Qiu,*[c] Yongfan Zhang,[d] Yayong Sun,[a] Wen-Hua Li,[a] Jian-Ze Xiao,[a] Jie Chen,[a] Gang Xu,*[abe] and Qipu Lin*[aef]

[a]*State Key Laboratory of Structural Chemistry, Fujian Provincial Key Laboratory of Materials and Techniques toward Hydrogen Energy, Fujian Institute of Research on the Structure of Matter, Chinese Academy of Sciences, Fuzhou, Fujian 350002, China*

[b]*Fujian Science & Technology Innovation Laboratory for Optoelectronic Information of China, Fuzhou, Fujian 350108, China*

[c]*College of Chemistry and Materials, Jiangxi Agricultural University, Nanchang, Jiangxi 330045, China*

[d]*College of Chemistry, Fuzhou University, Fuzhou, Fujian 350116, China*

[e]*University of Chinese Academy of Sciences, Beijing 100049, China*

[f]*State Key Laboratory of Photocatalysis on Energy and Environment, Fuzhou University, Fuzhou, Fujian 350116, China*

Corresponding author E-mail: qium@jxau.edu.cn; gxu@fjirsm.ac.cn; linqipu@fjirsm.ac.cn

Table of Contents

Section 1: General Methods

Chemicals: The chemicals were commercially available without further purification. 3,4-dimethoxybenzaldehyde and pyrrole were purchased from TCI (Shanghai) Development Co., Ltd. Boron tribromide (BBr_3), $FeCl_2$, $CoCl_2·6H_2O$, $Ni(NO_3)_2·6H_2O$ and $Zn(NO_3)_2·6H_2O$ were obtained from Aladdin (Shanghai) Development Co., Ltd. $FeCl_2·4H_2O$ was supplied by Shanghai Macklin Biochemical Co., Ltd. Ethanol, methanol, dichloromethane, trichloromethane, propionic acid, *N,N*-dimethylformamide and $In(NO_3)_3·4.5H_2O$ were purchased from Sinopharm Chemical Reagent Co., Ltd. The target gas was provided by Beijing Hua Yuan Gas Chemical Industry Co., Ltd., China.

Instrumentations: The powder X-ray diffraction (PXRD) patterns of the samples were carried out on the Rigaku Dmax 2500 X-ray diffractometer with Cu Kα radiation (λ = 1.54056 Å). The gas adsorption measurements were performed on a Micromeritics ASAP 2020 surface area and pore size analyzer. The scanning electron microscopy (SEM) images were obtained by a Zeiss Sigma 500. Surface chemical analysis was performed on the X-ray photoelectron spectrometer (Thermo Fisher Scientific ESCALAB 250Xi). The interdigital electrodes of the sensor substrates which were provided by Beijing Elite Tech Co., Ltd.

Section 2: The Syntheses of Ligands

Synthesis of 5,10,15,20-tetrakis(3,4-dihydroxyphenyl)porphyrin-Fe (3,4-TDHPP-Fe): 3,4-TDHPP-Fe was synthesized based on the previous literatures.[1-3] 3,4-TDMPP (1 mmol, 0.855 g, the synthesis method refers to our previous work[1]) and $FeCl_2·4H_2O$ (10 mmol, 1.99 g) were dissolved 150 ml CH_2Cl_2 and 30 ml CH_3OH, respectively. Then the solution was mixed and refluxed under Ar atmosphere for 24 h. After cooling down to room temperature, the mixture was transferred into the separatory funnel and then 300 mL H_2O was introduced for 3 times to remove excess $FeCl_2$. The purple powder was obtained after the CH_2Cl_2 solution was removed by evaporating, named 3,4-TDMPP-Fe. Then 3,4-TDMPP-Fe (1 mmol, 0.908 g) was dissolved in 20 mL

CH_2Cl_2. 1.5 mmol BBr_3 solution (1 mol/L in CH_2Cl_2) was added into 3,4-TDMPP-Fe solution under N_2 atmosphere by syringe at -78 °C and the reaction was maintained at -78 °C for 24 h. Then the reaction was terminated by adding 50 mL water after the reaction temperature rising naturally to room temperature. The solvents were removed by filtration and drying. Then olive-green product was obtained, named 3,4-TDHPP-Fe.

Synthesis of 5,10,15,20-tetrakis(3,4-dihydroxyphenyl)porphyrin-M (3,4-TDHPP-M, M = Co, Ni and Zn): The synthetic procedures of 3,4-TDHPP-M (M = Co, Ni and Zn) are similar to that of 3,4-TDHPP-Fe, except for $CoCl_2 \cdot 6H_2O$, $NiCl_2 \cdot 6H_2O$ and $Zn(NO_3)_2 \cdot 6H_2O$ instead of $FeCl_2 \cdot 4H_2O$, respectively.

Section 3 The Synthesis of Crystalline Compounds

Synthesis of FeTCP-M (M = Fe, Co, Ni and Zn)

The synthetic methods of FeTCP-M (M = Fe, Co, Ni and Zn) were similar to that in the previous literature[1] with some modification. $FeCl_2$ (0.075 mmol, 0.0095 g), 3,4-TDHPP-Fe (0.075 mmol, 0.0597 g), *N, N*-dimethylformamide (DMF, 3.0 mL), water (0.5 mL) and methanol (0.5 ml) were mixed in a 23 mL teflon-lined stainless steel container, then heated to 140 °C for 4 days. After cooling to room temperature, brown power was obtained after washing with methanol and drying, named FeTCP-Fe (81% yield based on 3,4-TDHPP-Fe). The synthetic methods of FeTCP-M (M = Co, Ni and Zn) were similar to that of FeTCP-Fe, except for 3,4-TDHPP-Co (0.075 mmol, 0.0599 g), 3,4-TDHPP-Ni (0.075 mmol, 0.0599 g) and 3,4-TDHPP-Zn (0.075 mmol, 0.0604 g) instead of 3,4-TDHPP-Fe (0.075 mmol, 0.0597 g), respectively. The yields of FeTCP-M were over 80% based on 3,4-TDHPP-M (M = Co, Ni and Zn). ICP data: FeTCP-Fe, Fe (9.93%); FeTCP-Co, Fe (7.92%), Co (2.12%); FeTCP-Ni, Fe (8.00%), Ni (1.93%); FeTCP-Zn, Fe (8.34%), Zn (1.87%).

Synthesis of InTCP-M (M = Fe, Co, Ni and Zn)

The synthetic methods of InTCP-M (M = Fe, Co, Ni and Zn) were similar to that in the previous literature[1] with some modification. $In(NO_3)_3 \cdot 4.5H_2O$ (0.075 mmol, 0.286 g), 3,4-TDHPP-Fe (0.075 mmol, 0.0597 g), water (1 ml) and *N,N*-

dimethylformamide (DMF, 3 mL) were mixed in a 23 mL teflon-lined stainless steel container, then heated to 140 °C for 4 days. After cooling to room temperature, brown power was obtained after washing with methanol and drying, named InTCP-Fe (75%, yield based on 3,4-TDHPP-Fe). The synthetic methods of InTCP-M (M = Co, Ni and Zn) were similar to that of InTCP-Fe, except for 3,4-TDHPP-Co (0.075 mmol, 0.0599 g), 3,4-TDHPP-Ni (0.075 mmol, 0.0599 g) and 3,4-TDHPP-Zn (0.075 mmol, 0.0604 g) instead of 3,4-TDHPP-Fe (0.075 mmol, 0.0597 g), respectively. The yields of InTCP-M were over 70% based on 3,4-TDHPP-M (M = Co, Ni and Zn). ICP data: InTCP-Fe, In (16.54%), Fe (2.22%); InTCP-Co, In (17.03%), Co (1.86%); InTCP-Ni, In (17.05%), Ni (1.58%); InTCP-Zn, In (17.05%), Zn (1.43%).

Section 4 Powder X-ray Diffraction (PXRD)

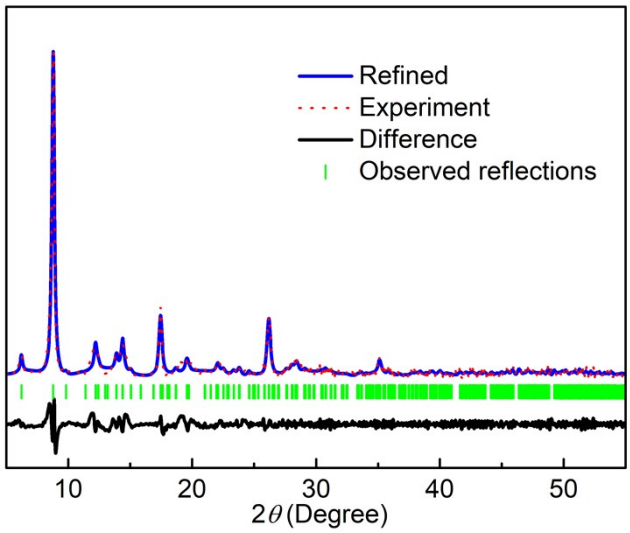

Fig. S1 The experimentally obtained and the Rietveld-refined PXRD patterns of InTCP-Fe.

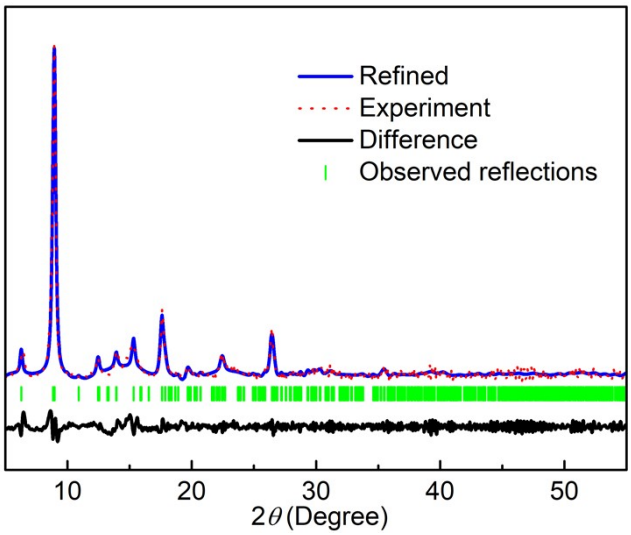

Fig. S2 The experimentally obtained and the Rietveld-refined PXRD patterns of FeTCP-Fe.

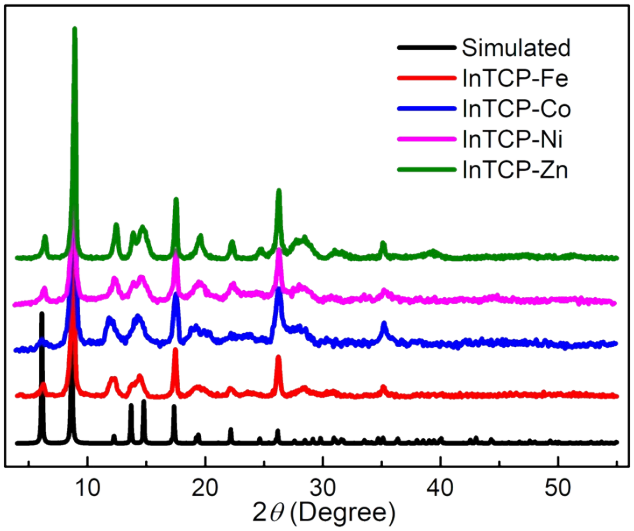

Fig. S3 The PXRD patterns of InTCP-M (M = Fe, Co, Ni and Zn).

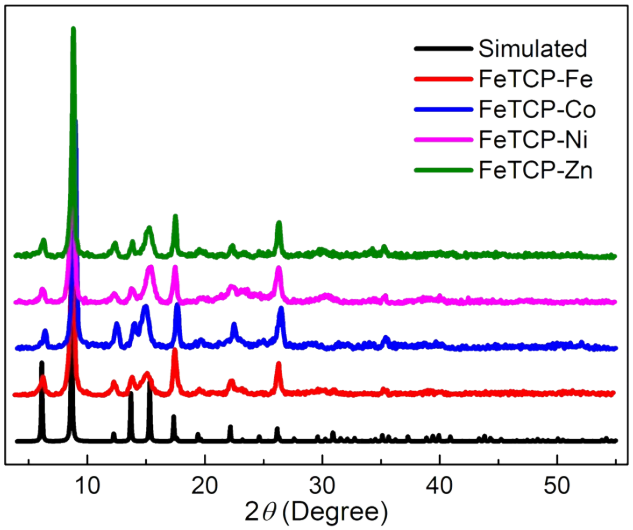

Fig. S4 The PXRD patterns of FeTCP-M (M = Fe, Co, Ni and Zn).

Section 5 The Morphology Characterization

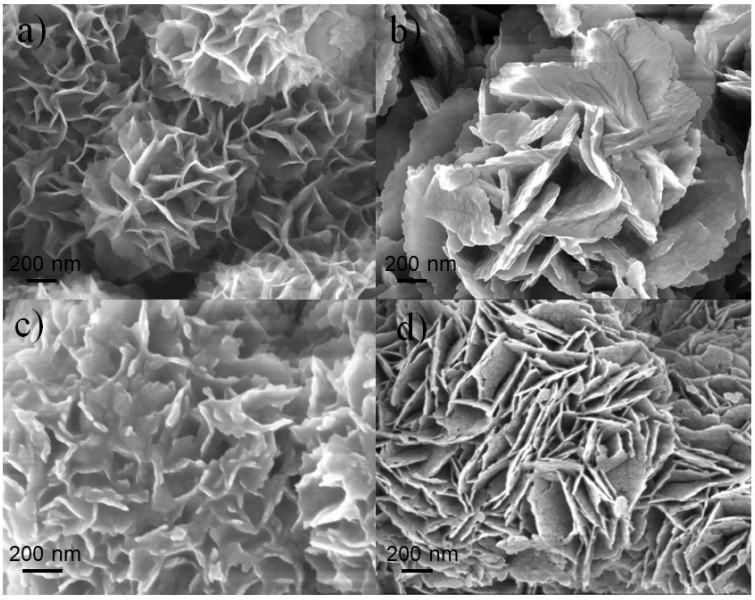

Fig. S5 The SEM images of InTCP-M with the scale bar of 200 nm, (a) InTCP-Fe; (b) InTCP-Co; (c) InTCP-Ni and (d) InTCP-Zn.

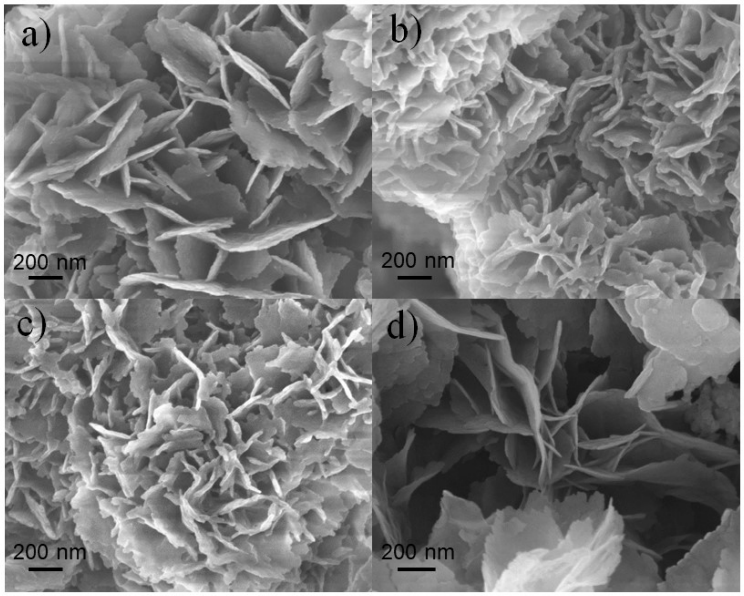

Fig. S6 The SEM images of FeTCP-M with the scale bar of 200 nm, (a) FeTCP-Fe; (b) FeTCP-Co; (c) FeTCP-Ni and (d) FeTCP-Zn.

Section 6 Gas Adsorption Measurements

Before the gas absorption measurement, InTCP-M and FeTCP-M (M = Fe, Co, Ni and Zn) were activated by soaking in CH_3OH three days and CH_3OH was renewed every 12 hours, respectively.

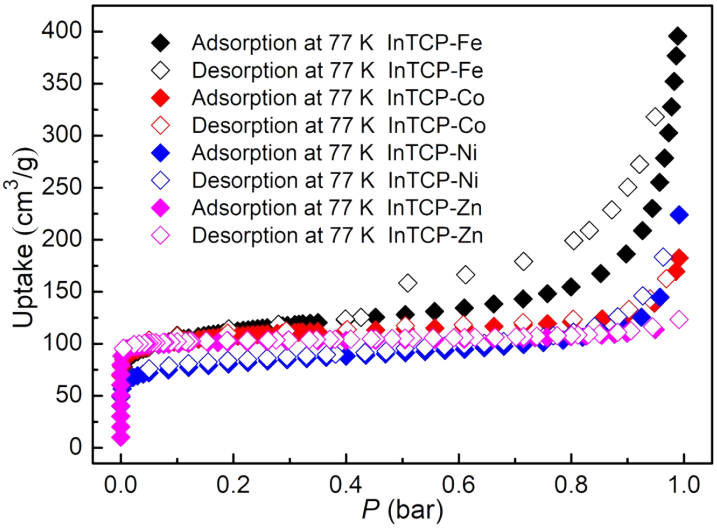

Fig. S7 N_2 adsorption/desorption isotherms of InTCP-M (M = Fe, Co, Ni and Zn) at 77 K.

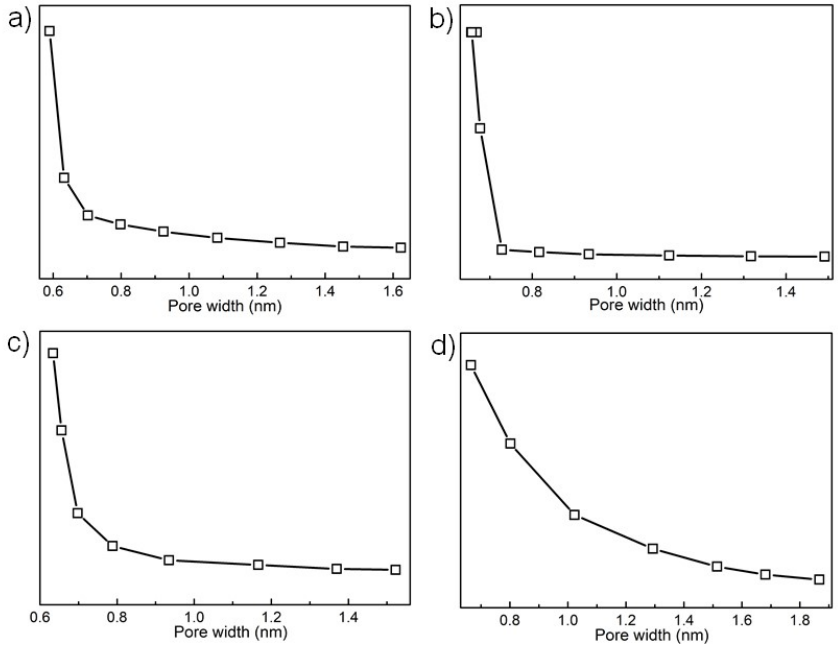

Fig. S8 The pore size distribution of (a) InTCP-Fe; (b) InTCP-Co; (c) InTCP-Ni; (d) InTCP-Zn.

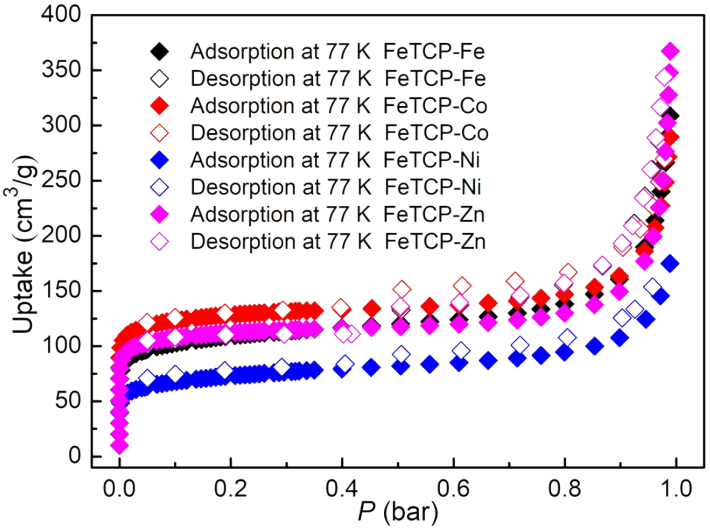

Fig. S9 N_2 adsorption/desorption isotherms of FeTCP-M (M = Fe, Co, Ni and Zn) at 77 K.

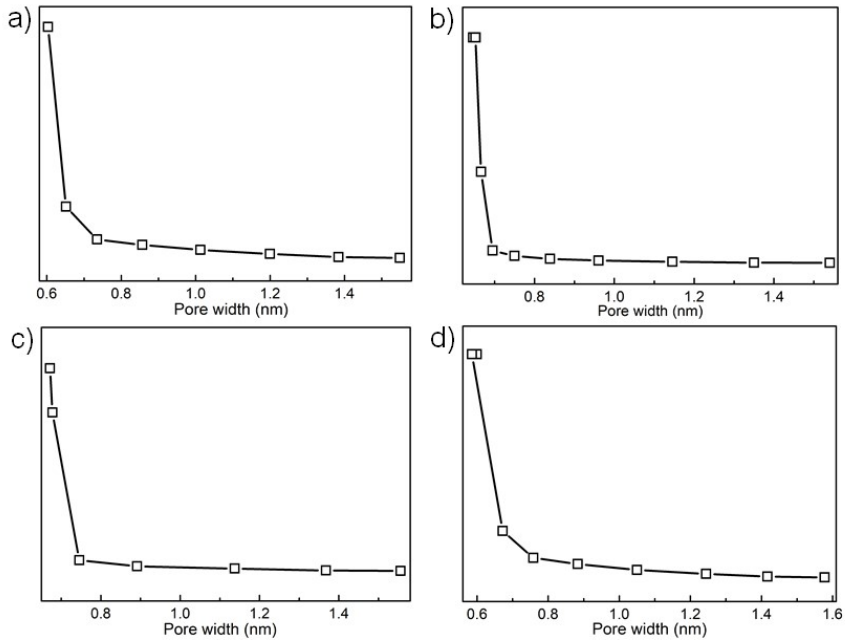

Fig. S10 The pore size distribution of (a) FeTCP-Fe; (b) FeTCP-Co; (c) FeTCP-Ni; (d) FeTCP-Zn.

Table S1. The BET and Langmuir surface areas and pore size distribution of (In/Fe)TCP-M (M = Fe, Co, Ni and Zn)

	BET (m^2 g^{-1})	Langmuir (m^2 g^{-1})	Pore size (nm)
InTCP-Fe	343.59	549.48	0.5896
InTCP-Co	317.76	500.88	06687
InTCP-Ni	249.68	387.28	0.6338
InTCP-Zn	290.73	450.95	0.6655

FeTCP-Fe	328.31	520.51	0.6031
FeTCP-Co	375.85	589.78	0.6500
FeTCP-Ni	223.22	356.11	0.6716
FeTCP-Zn	328.18	514.89	0.5900

Section 7 Ultraviolet-Visible (UV-vis) Absorption Spectroscopy

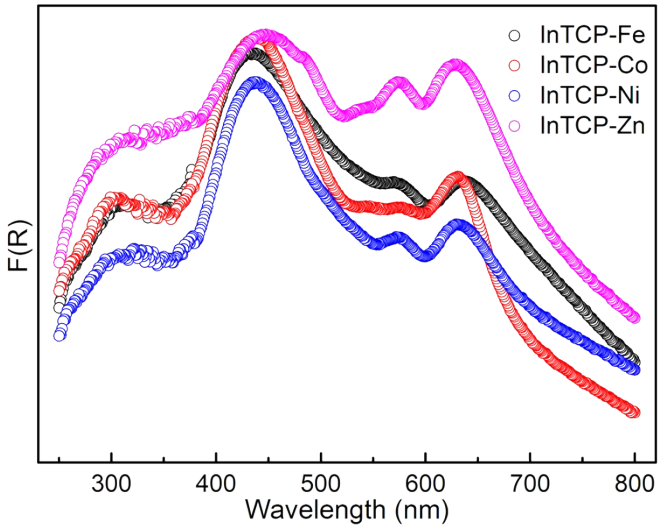

Fig. S11 The UV-vis diffuse-reflectance spectra of InTCP-M (M = Fe, Co, Ni and Zn).

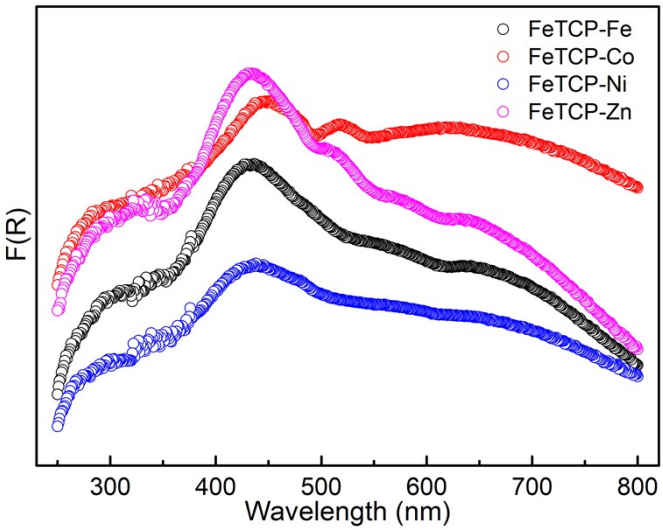

Fig. S12 The UV-vis diffuse-reflectance spectra of FeTCP-M (M = Fe, Co, Ni and Zn).

Section 8 Gas Sensing Characterization

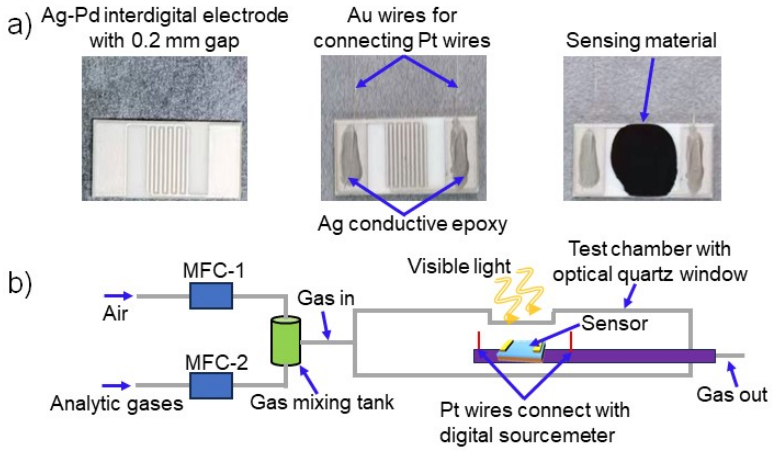

Fig. S13 (a) Photographs of sensor devices in this work; (b) Schematic illustration of the custom-built gas-sensing instrument with a dynamic gas distribution system at room temperature and under visible light irradiation.

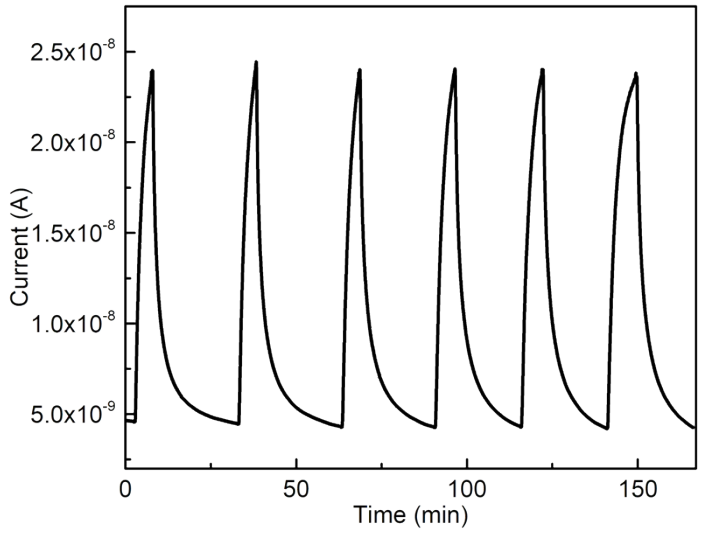

Fig. S14 The dynamic response-recovery curve of InTCP-Fe to 10 ppm NO_2 in the six consecutive cycles with the visible light irradiation.

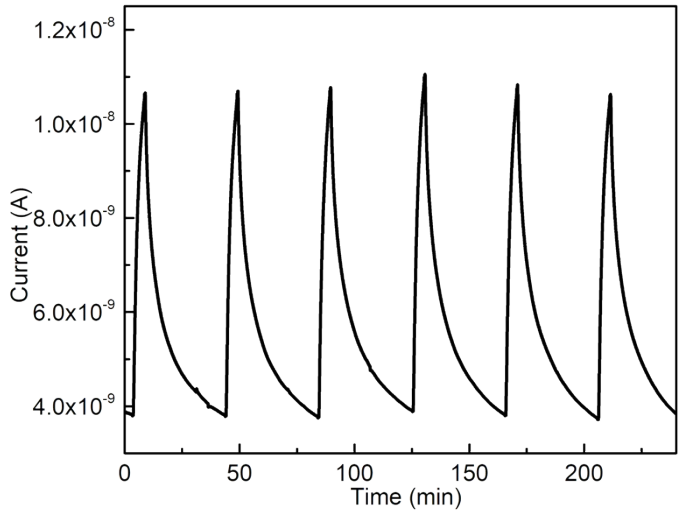

Fig. S15 The dynamic response-recovery curve of InTCP-Ni to 10 ppm NO_2 in the six consecutive cycles with the visible light irradiation.

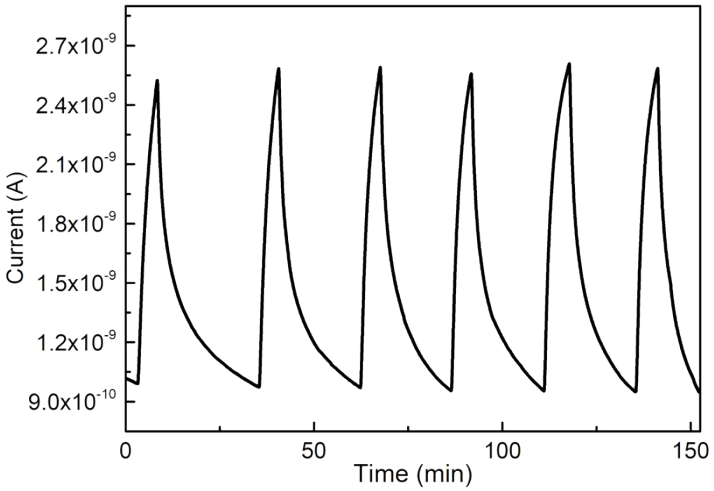

Fig. S16 The dynamic response-recovery curve of InTCP-Zn to 10 ppm NO_2 in the six consecutive cycles with the visible light irradiation.

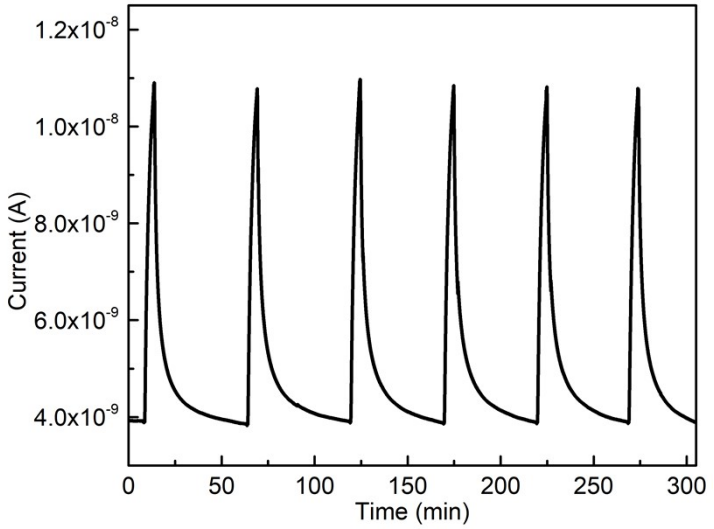

Fig. S17 The dynamic response-recovery curve of FeTCP-Fe to 10 ppm NO_2 in the six consecutive cycles with the visible light irradiation.

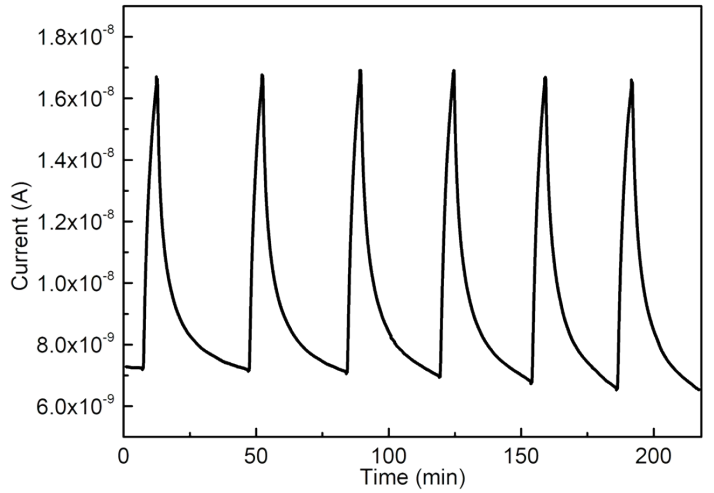

Fig. S18 The dynamic response-recovery curve of FeTCP-Co to 10 ppm NO_2 in the six consecutive cycles with the visible light irradiation.

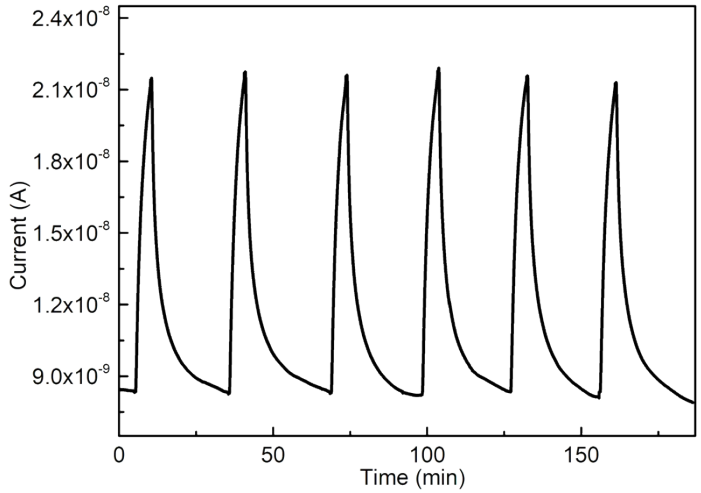

Fig. S19 The dynamic response-recovery curve of FeTCP-Ni to 10 ppm NO_2 in the six consecutive cycles with the visible light irradiation.

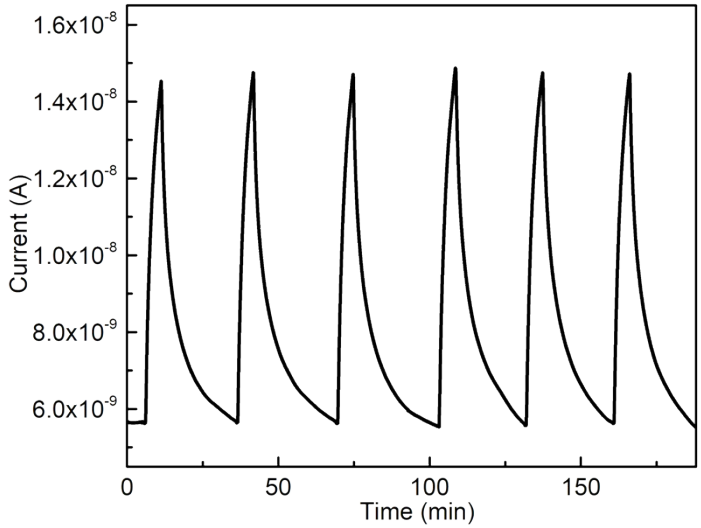

Fig. S20 The dynamic response-recovery curve of FeTCP-Zn to 10 ppm NO_2 in the six consecutive cycles with the visible light irradiation.

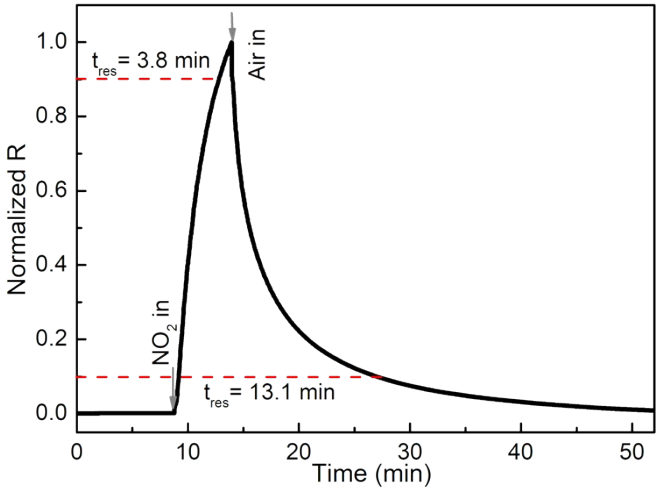

Fig. S21 The normalized response-recovery time curve of InTCP-Co to 10 ppm NO_2 with the visible light irradiation.

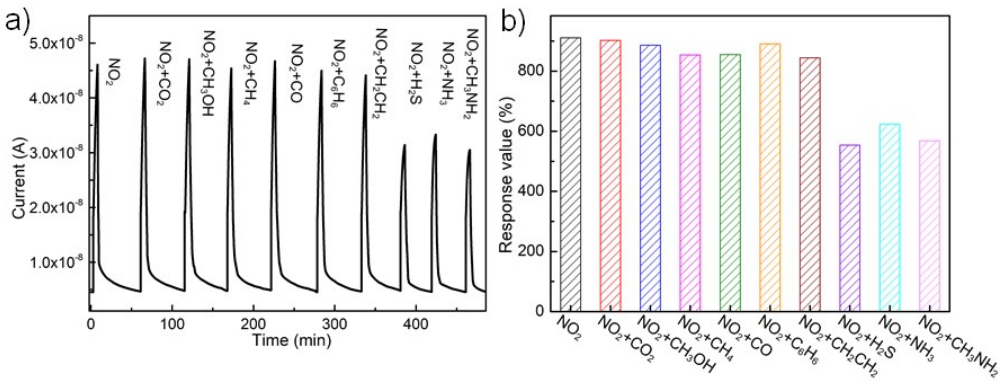

Fig. S22 (a) The dynamic response-recovery curve of InTCP-Co to 10 ppm NO_2 and 10ppm NO_2 mixed with 10ppm other gases; (b) The response values of InTCP-Co to 10 ppm NO_2 and 10ppm NO_2 mixed with 10ppm other gases.

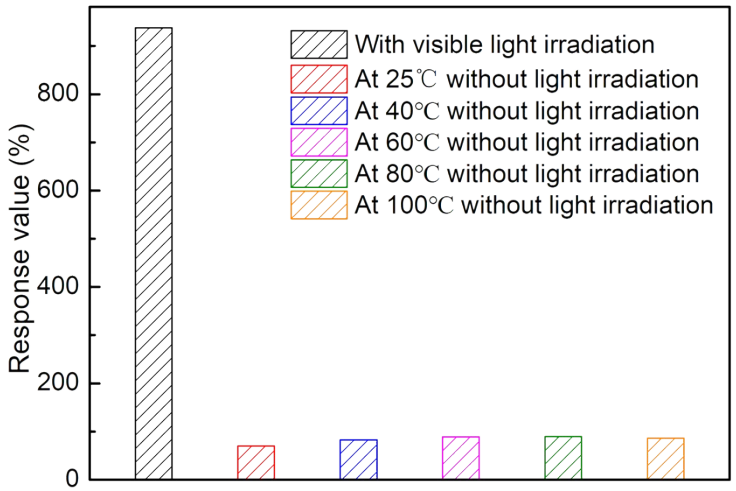

Fig. S23 The response values of InTCP-Co to 10 ppm NO_2 under the visible light irradiation and at different temperature without light irradiation.

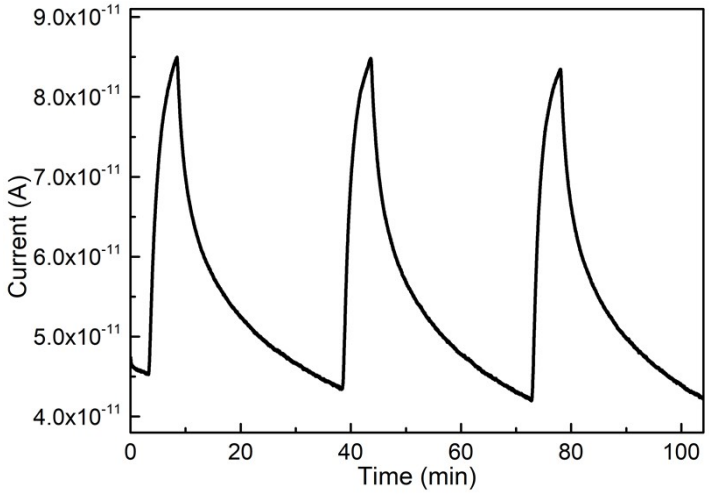

Fig. S24 The dynamic response-recovery curve of InTCP-Co to 10 ppm NO_2 in three consecutive cycles at room temperature (25 ℃) without light irradiation.

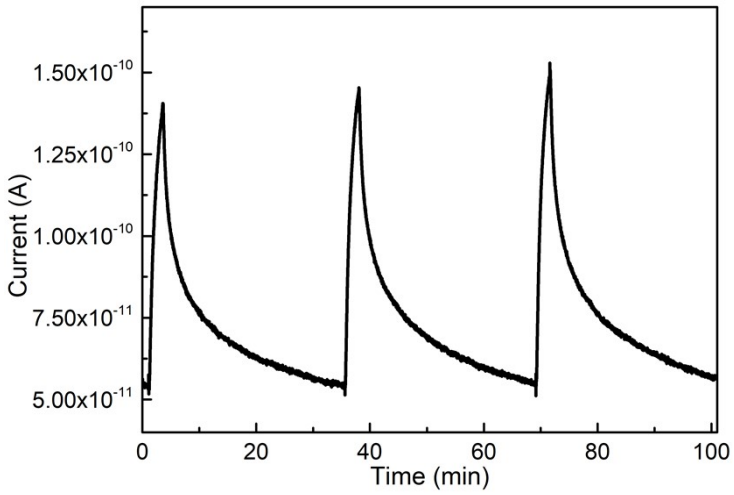

Fig. S25 The dynamic response-recovery curve of InTCP-Co to 10 ppm NO_2 in three consecutive cycles at 40 ℃ without light irradiation.

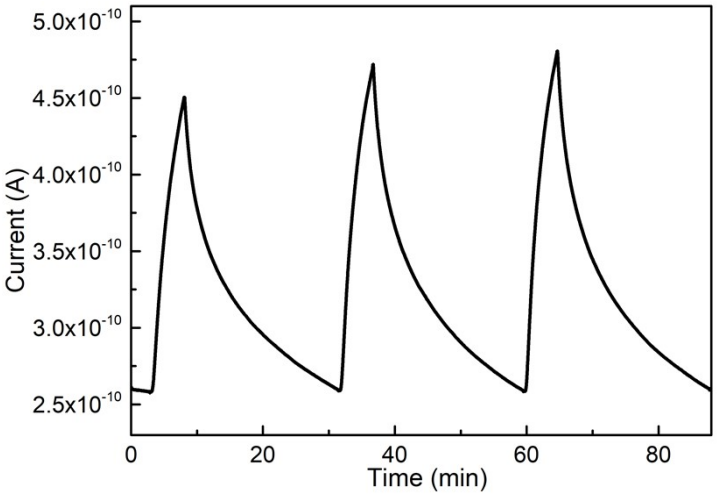

Fig. S26 The dynamic response-recovery curve of InTCP-Co to 10 ppm NO_2 in three consecutive cycles at 60 ℃ without light irradiation.

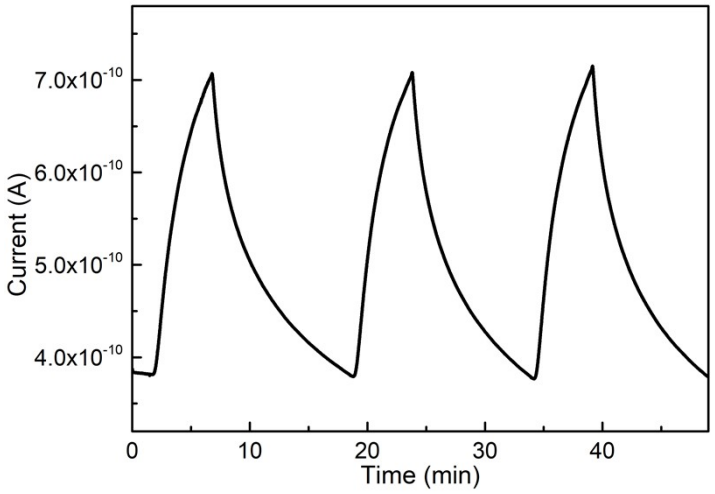

Fig. S27 The dynamic response-recovery curve of InTCP-Co to 10 ppm NO_2 in three consecutive cycles at 80 ℃ without light irradiation.

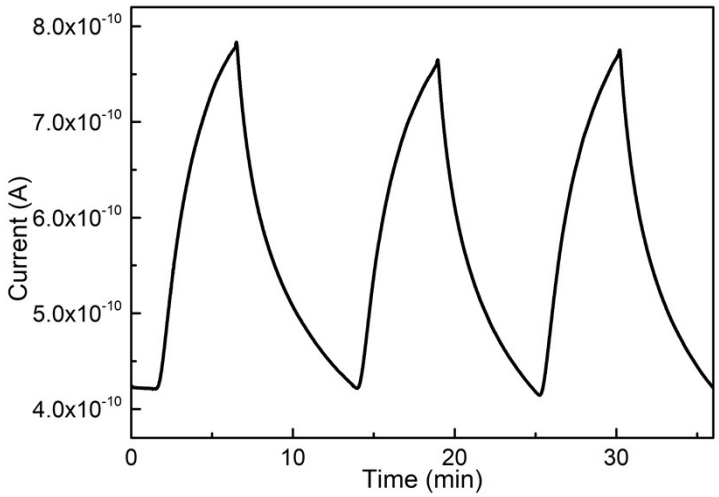

Fig. S28 The dynamic response-recovery curve of InTCP-Co to 10 ppm NO_2 in three consecutive cycles at 100 ℃ without light irradiation.

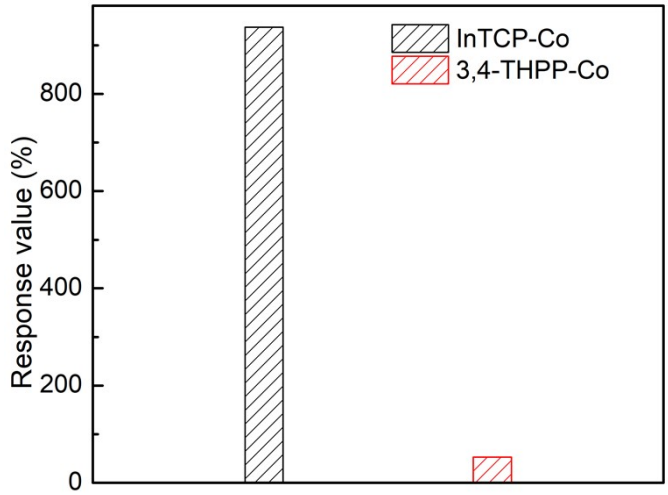

Fig. S29 The response values of InTCP-Co and 3,4-TDHPP-Co to 10 ppm NO_2 under the visible light irradiation.

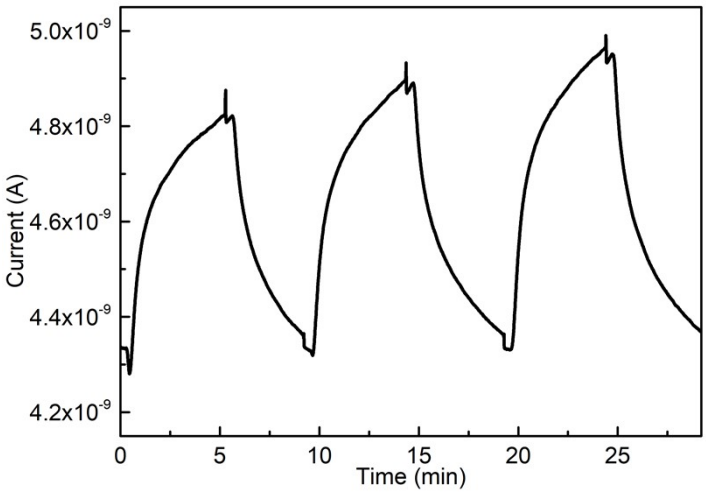

Fig. S30 The dynamic response-recovery curve of 3,4-TDHPP-Co to 10 ppm NO_2 in three consecutive cycles with the visible light irradiation.

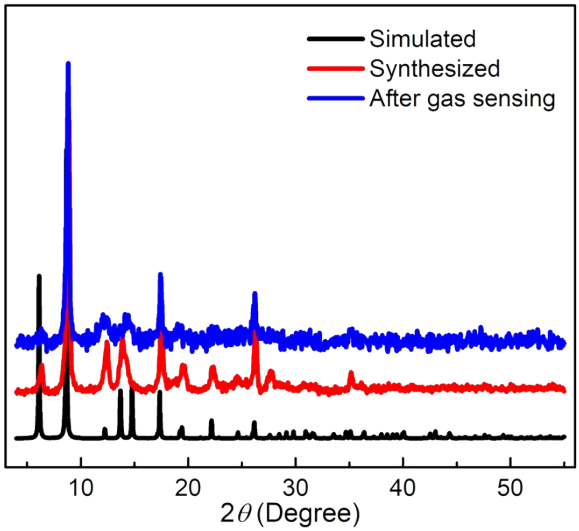

Fig. S31 The PXRD patterns of InTCP-Co after the gas sensing tests.

Table S2 Gas sensing properties of reported materials for the NO_2 under room temperature and visible-light irradiation

Material	Concentration	Response	$T_{res.}/T_{rec.}$	Experimental detection limit	Long-term stability	Ref.
Zn-TDCOF-12	100 ppm	554	8.1 min/10.6 min	40 ppb	35 days	4
FIR-120	10 ppm	2040%	2.48 min/2.60 min	40 ppb	70 days	5
HOF-1	100 ppm	1.7×10^5%	2.5 min/0.6 min	20 ppb	50 days	6
HOF-2	100 ppm	4.0×10^4%	3.8 min/2.0 min	40 ppb	-	6
HOF-3	100 ppm	4.5×10^3%	5.7 min/5.8 min	40 ppb	-	6
HPS $WO_3/CuWO_4$	1 ppm	82	93 s/28 s	50 ppb	30 days	7
WO_3	160 ppb	2.9	14.9 min/18.3 min	-	-	8
dye sensitized a-ZnO	1.25 ppm	1.25	long/long	1.25 ppm	-	9
3D IO In_2O_3–ZnO HCMs (S3)	5 ppm	54.3	586 s/188 s	250 ppb	30 days	10
Black NiO	372 ppb	31.04%	13.2 min/29.1 min	57 ppb	-	11
r-GO-ZnO	100 ppb	4.66	1.5 min/2.5 min	50 ppb	30 days	12
PI/SnO_2	0.5 ppm	131.6	6 min/4 min	250 ppb	-	13
Rb_2CO_3/In_2O_3	250 ppb	60	2.5 min/~45 min	150 ppb	45 days	14
SnO_2@SnS_2	0.2 ppm	5.3	950 s/1160 s	0.2 ppm	180 days	15
ZnO/g-C_3N_4-10wt%	7 ppm	44.8	142 s/190 s	100 ppb	-	16
ZnO/Pd	100 ppb	~160%	25 s/29 s	5 ppb	90 days	17
In_2O_3	500 ppb	5.52	~500 s/1100 s	10 ppb	90 days	18
ReS_2 nanosheets	500 ppb	9.07	55 s/180 s	50ppb	40 days, (about 12% decay)	19
SnS_2 NFs	5 ppm	14.28	400 s/1100 s	400 ppb	90 days	20

ZIC	1 ppm	7.2	36 s/80 s	50 ppb	40 days	21
Fe_2O_3–Cu_3(HHTP)$_2$-NFs	5 ppm	63.5%	~27 min/~100 min	200 ppb	-	22
5Au–SnO_2	5 ppm	180	500 s/223 s	125 ppb	30 days	23
Ti_3C_2Tx/WS_2	2 ppm	55.6%	56 s/53 s	10 ppb	90 days	24
S-doped SnO_2 NPs	5 ppm	418	170 s/64 s	200 ppb	90 days (about 16% decay)	25
Au/WS_2	1 ppm	~4.1	~50 s/~83 s	20 ppb	30 days	26
Bi_2S_3/SnS_2	500 ppb	14	38 s/80 s	50 ppb	50 days	27
[*n*-pentylaminium]$_2$[ethylammonium]$_2Pb_3I_{10}$	5 ppm	34%	9 s/9.6 s	1 ppm	3 days	28
InTCP-Co	10 ppm	937%	3.8 min/13.1 min	40 ppb	90 days	This work

Section 9 X-ray Photoelectron Spectroscopy (XPS)

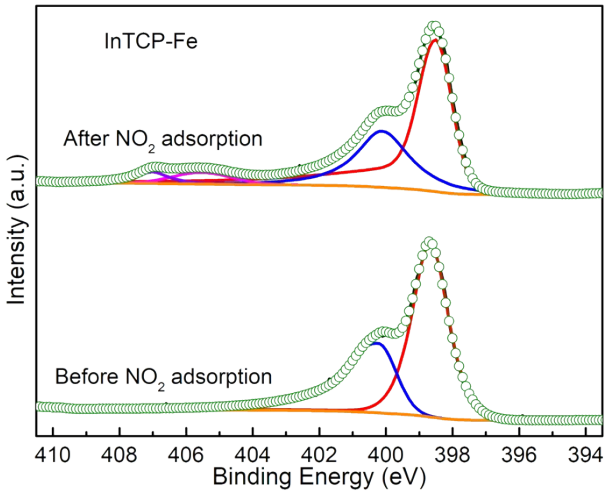

Fig. S32 The N1s XPS spectra of InTCP-Fe before and after NO_2 adsorption.

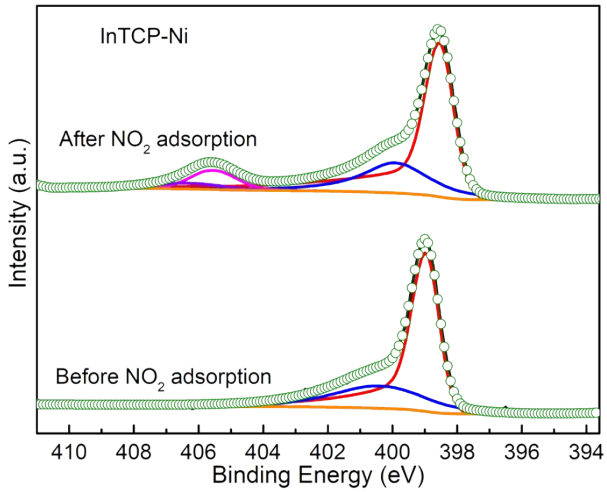

Fig. S33 The N1s XPS spectra of InTCP-Ni before and after NO_2 adsorption.

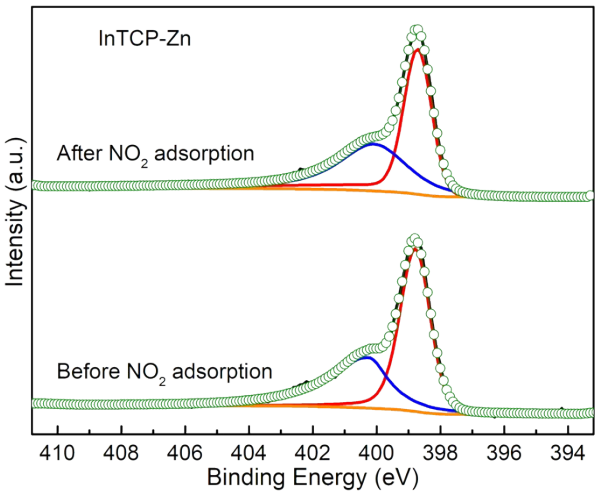

Fig. S34 The N1s XPS spectra of InTCP-Zn before and after NO_2 adsorption.

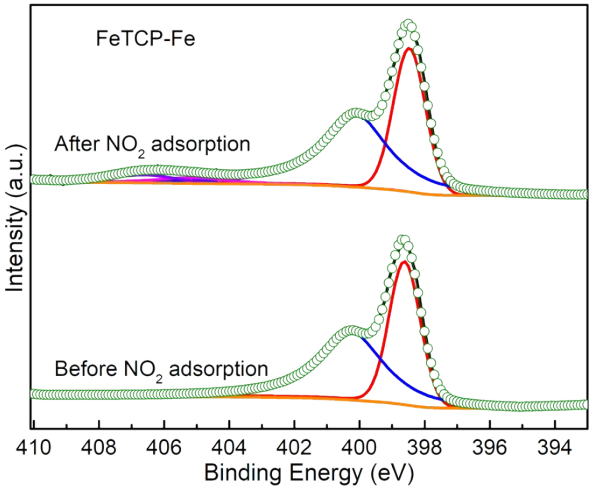

Fig. S35 The N1s XPS spectra of FeTCP-Fe before and after NO_2 adsorption.

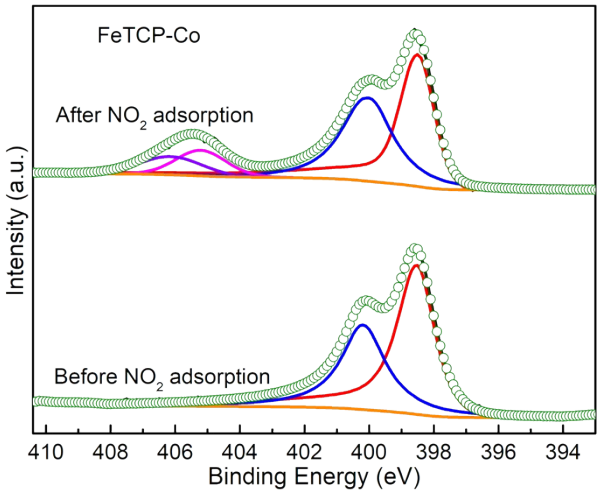

Fig. S36 The N1s XPS spectra of FeTCP-Co before and after NO_2 adsorption.

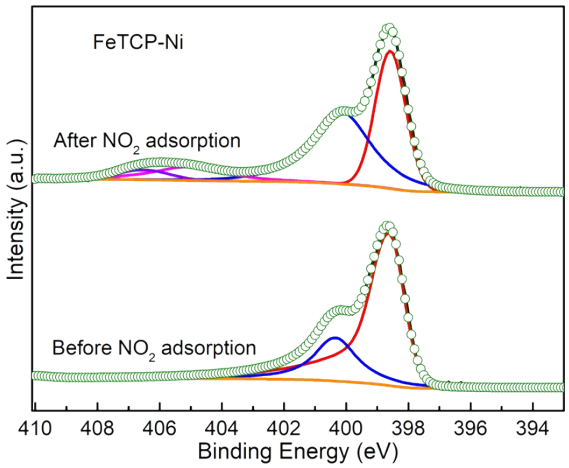

Fig. S37 The N1s XPS spectra of FeTCP-Ni before and after NO_2 adsorption.

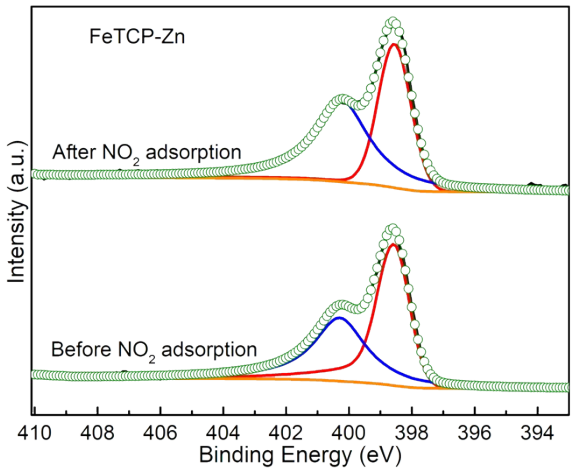

Fig. S38 The N1s XPS spectra of FeTCP-Zn before and after NO_2 adsorption.

Section 10 Density Functional Theory (DFT) Calculations

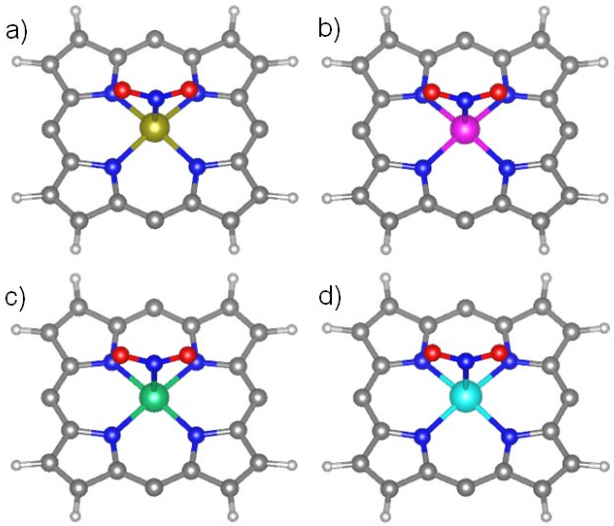

Fig. S39 The optimal NO_2 adsorption configurations on (a) FeTCP-Fe; (b) FeTCP-Co; (c) FeTCP-Ni and (d) FeTCP-Zn; The other parts in the structures of FeTCP-M (M = Fe, Co, Ni and Zn) have been omitted for clarity in the (a)~(d).

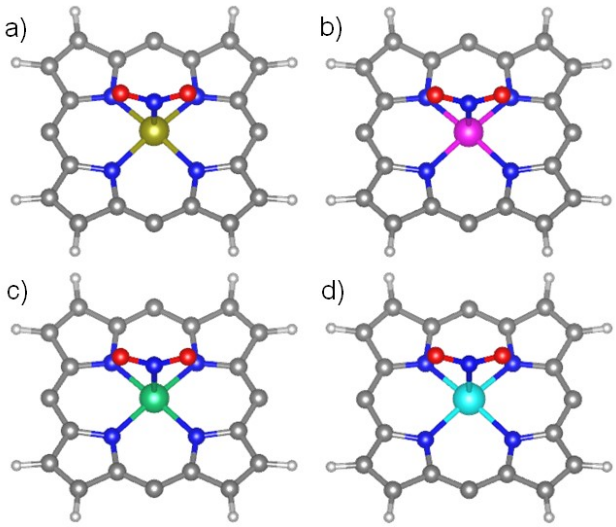

Fig. S40 The optimal NO_2 adsorption configurations on (a) InTCP-Fe; (b) InTCP-Co; (c) InTCP-Ni and (d) InTCP-Zn; The other parts in the structures of InTCP-M (M = Fe, Co, Ni and Zn) have been omitted for clarity in the (a)~(d).

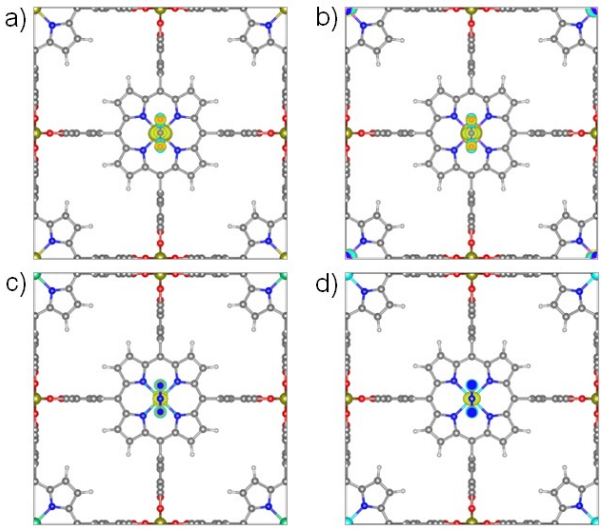

Fig. S41 The charge difference density maps of NO_2 adsorbed on (a) FeTCP-Fe; (b) FeTCP-Co; (c) FeTCP-Ni and (d) FeTCP-Zn.

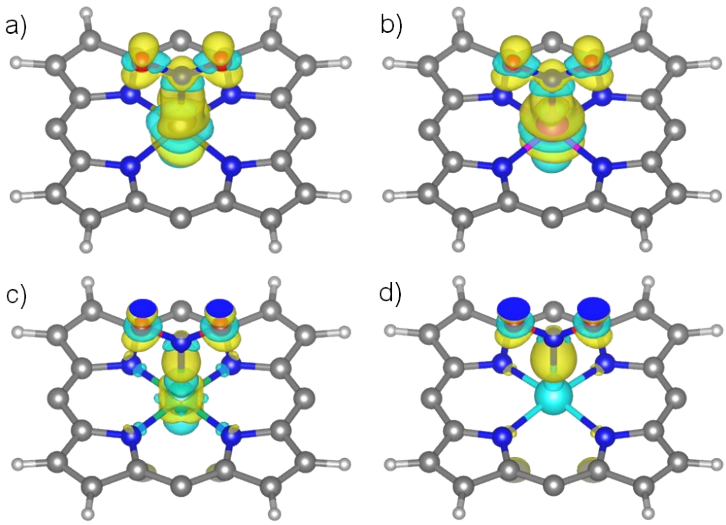

Fig. S42 The charge difference density maps of NO_2 adsorbed on (a) FeTCP-Fe; (b) FeTCP-Co; (c) FeTCP-Ni and (d) FeTCP-Zn; The other parts in the structures of FeTCP-M (M = Fe, Co, Ni and Zn) have been omitted for clarity in the (a)~(d).

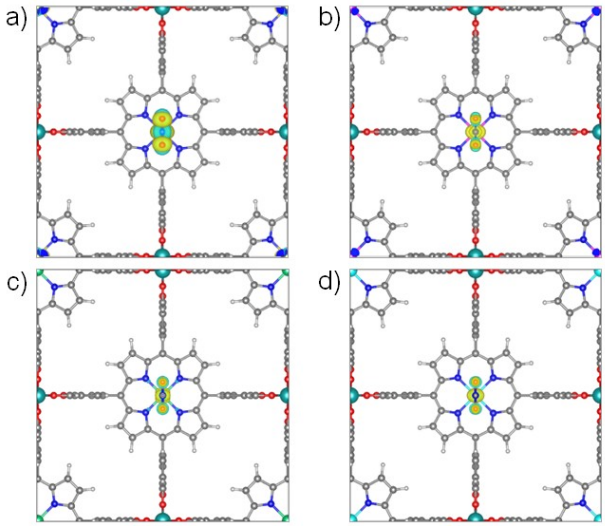

Fig. S43 The charge difference density maps of NO_2 adsorbed on (a) InTCP-Fe; (b) InTCP-Co; (c) InTCP-Ni and (d) InTCP-Zn.

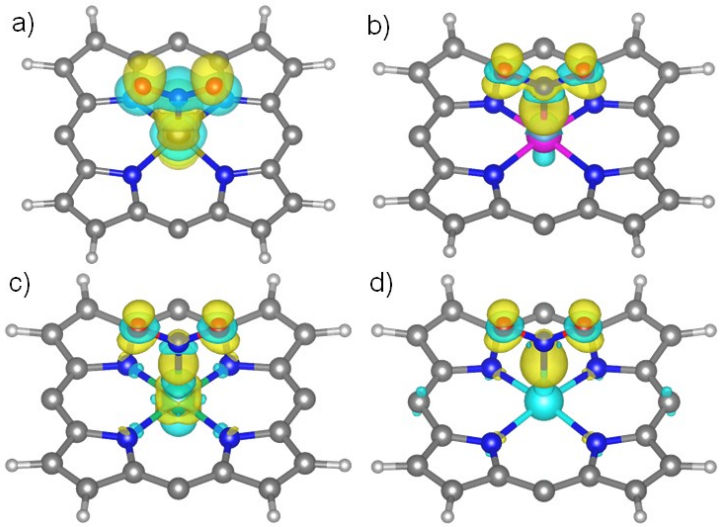

Fig. S44 The charge difference density maps of NO_2 adsorbed on (a) InTCP-Fe; (b) InTCP-Co; (c) InTCP-Ni and (d) InTCP-Zn; The other parts in the structures of InTCP-M (M = Fe, Co, Ni and Zn) have been omitted for clarity in the (a)~(d).

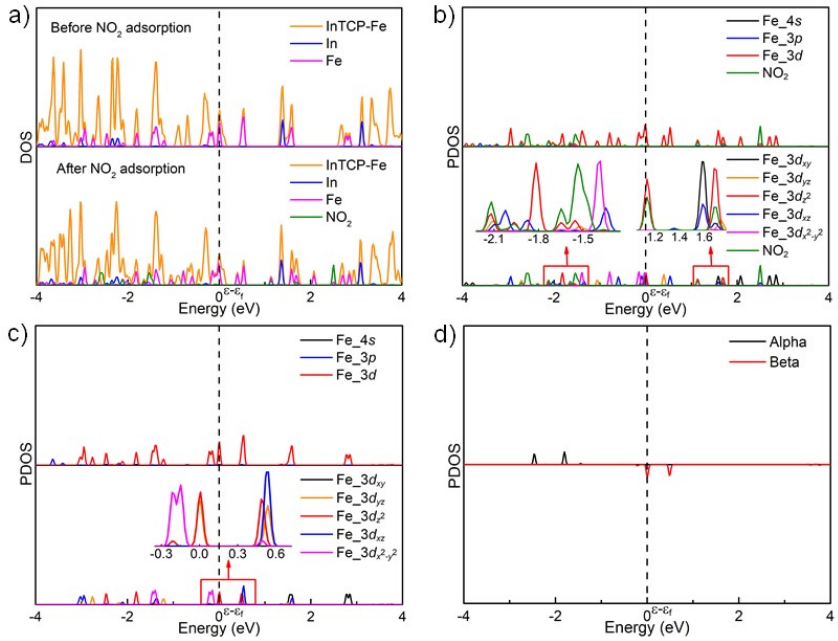

Fig. S45 (a) The TDOS and PDOS of InTCP-Fe before and after NO_2 adsorption; (b) The PDOS of NO_2 and Fe-4*s*, Fe-3*p*, Fe-3*d* orbitals of InTCP-Fe after NO_2 adsorption; (c) The PDOS of Fe-4*s*, Fe-3*p* and Fe-3*d* orbitals of InTCP-Fe before NO_2 adsorption; (d) The PDOS of electron spin states in Fe-3d_z^2 orbital of InTCP-Fe.

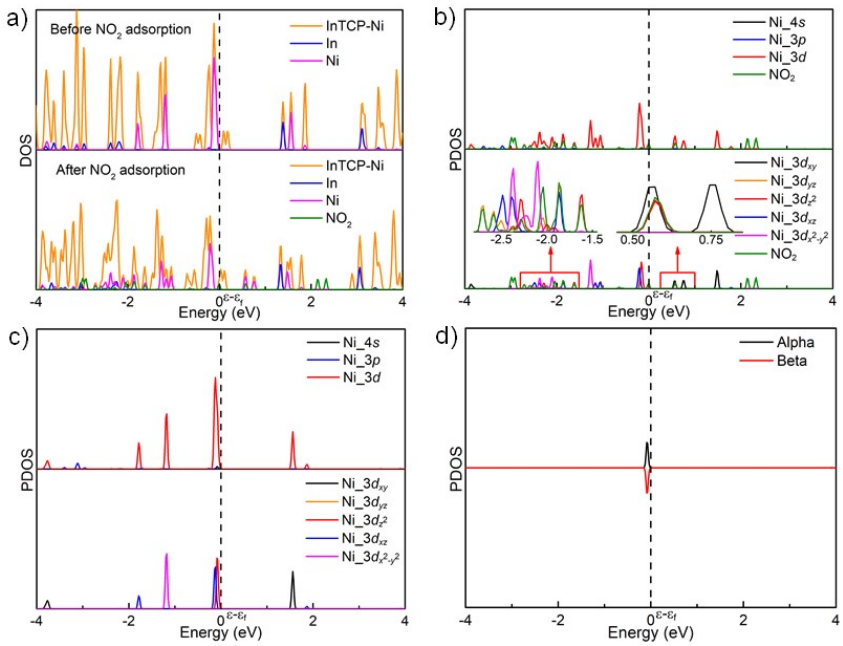

Fig. S46 (a) The TDOS and PDOS of InTCP-Ni before and after NO_2 adsorption; (b) The PDOS of NO_2 and Ni-4*s*, Ni-3*p*, Ni-3*d* orbitals of InTCP-Ni after NO_2 adsorption; (c) The PDOS of Ni-4*s*, Ni-3*p* and Ni-3*d* orbitals of InTCP-Ni before NO_2 adsorption; (d) The PDOS of electron spin states in Ni-3d_z^2 orbital of InTCP-Ni.

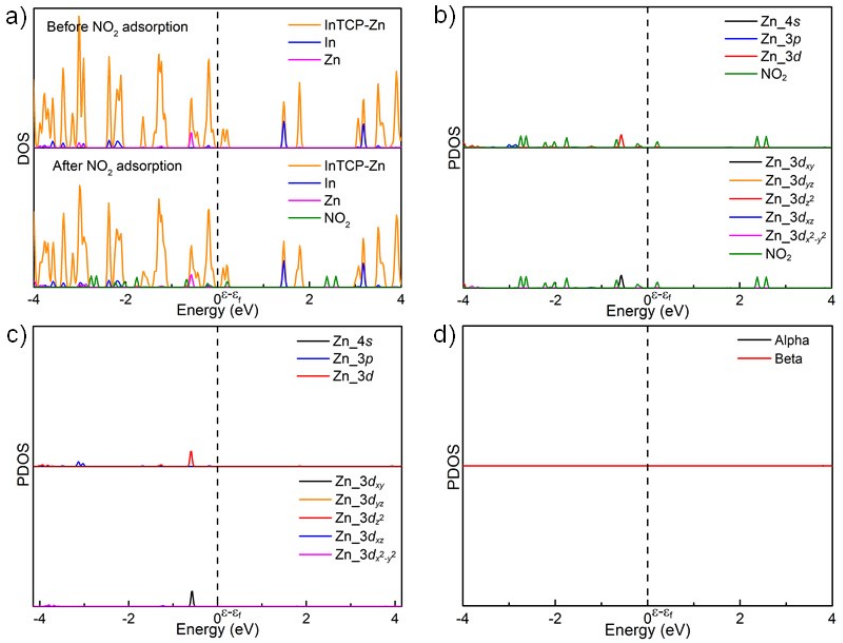

Fig. S47 (a) The TDOS and PDOS of InTCP-Zn before and after NO_2 adsorption; (b) The PDOS of NO_2 and Zn-4*s*, Zn-3*p*, Zn-3*d* orbitals of InTCP-Zn after NO_2 adsorption; (c) The PDOS of Zn-4*s*, Zn-3*p* and Zn-3*d* orbitals of InTCP-Zn before NO_2 adsorption; (d) The PDOS of electron spin states in Zn-3d_z^2 orbital of InTCP-Zn.

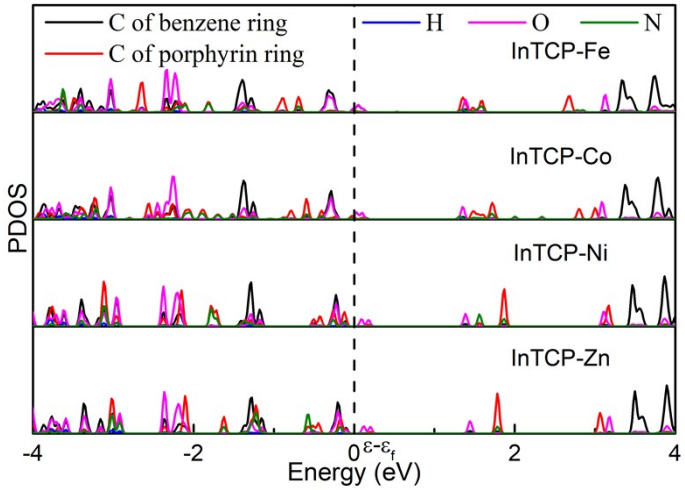

Fig. S48 The PDOS of C, H, O and N of InTCP-M before NO_2 adsorption (M = Fe, Co, Ni and Zn).

Table S3. The integrated crystal orbital overlap population (ICOOP) values between NO_2 and *beta* state of electron spin in M-3d_z^2 of InTCP-M and FeTCP-M (M = Fe, Co, Ni and Zn)

	ICOOP value		ICOOP value
InTCP-Fe	0.04833	FeTCP-Fe	0.05918
InTCP-Co	0.05263	FeTCP-Co	0.05072
InTCP-Ni	0.03688	FeTCP-Ni	0.03742
InTCP-Zn	0.00919	FeTCP-Zn	0.00995

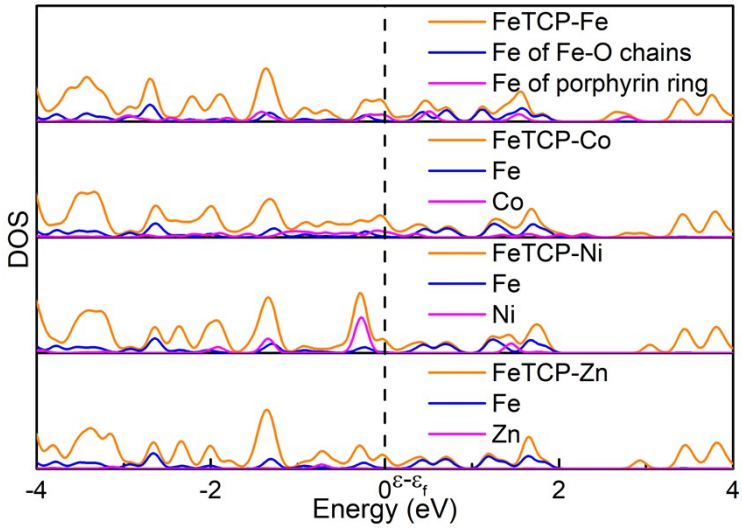

Fig. S49 The TDOS of FeTCP-M and PDOS of Fe and M in porphyrin ring before NO_2 adsorption (M = Fe, Co, Ni and Zn).

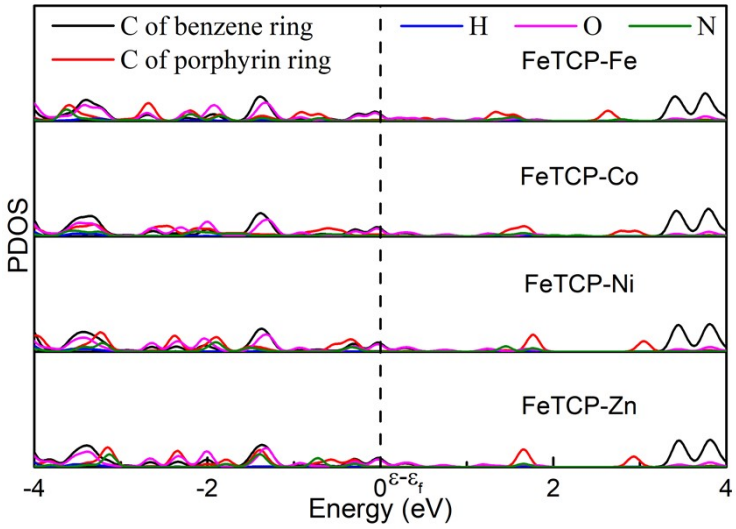

Fig. S50 The PDOS of C, H, O and N of FeTCP-M before NO_2 adsorption (M = Fe, Co, Ni and Zn).

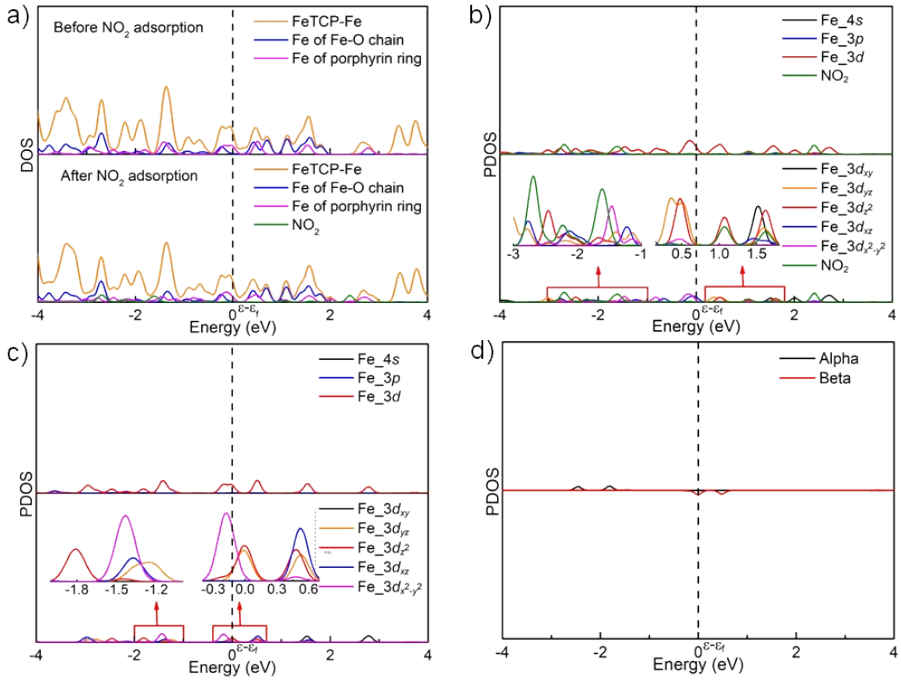

Fig. S51 (a) The TDOS and PDOS of FeTCP-Fe before and after NO_2 adsorption; (b) The PDOS of NO_2 and Fe-4*s*, Fe-3*p*, Fe-3*d* orbitals of Fe in porphyrin ring of FeTCP-Fe after NO_2 adsorption; (c) The PDOS of Fe-4*s*, Fe-3*p* and Fe-3*d* orbitals of Fe in porphyrin ring of FeTCP-Fe before NO_2 adsorption; (d) The PDOS of electron spin states in Fe-3d_z^2 orbital of Fe in porphyrin ring of FeTCP-Fe.

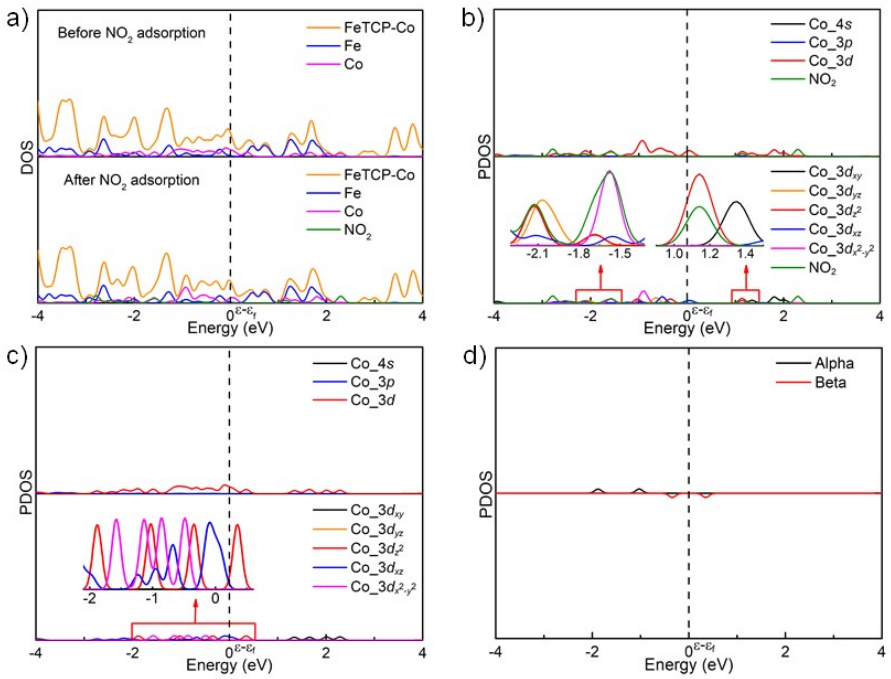

Fig. S52 (a) The TDOS and PDOS of FeTCP-Co before and after NO_2 adsorption; (b) The PDOS of NO_2 and Co-4*s*, Co-3*p*, Co-3*d* orbitals of FeTCP-Co after NO_2 adsorption; (c) The PDOS of Co-4*s*, Co-3*p* and Co-3*d* orbitals of FeTCP-Co before NO_2 adsorption; (d) The PDOS of electron spin states in Co-3d_z^2 orbital of FeTCP-Co.

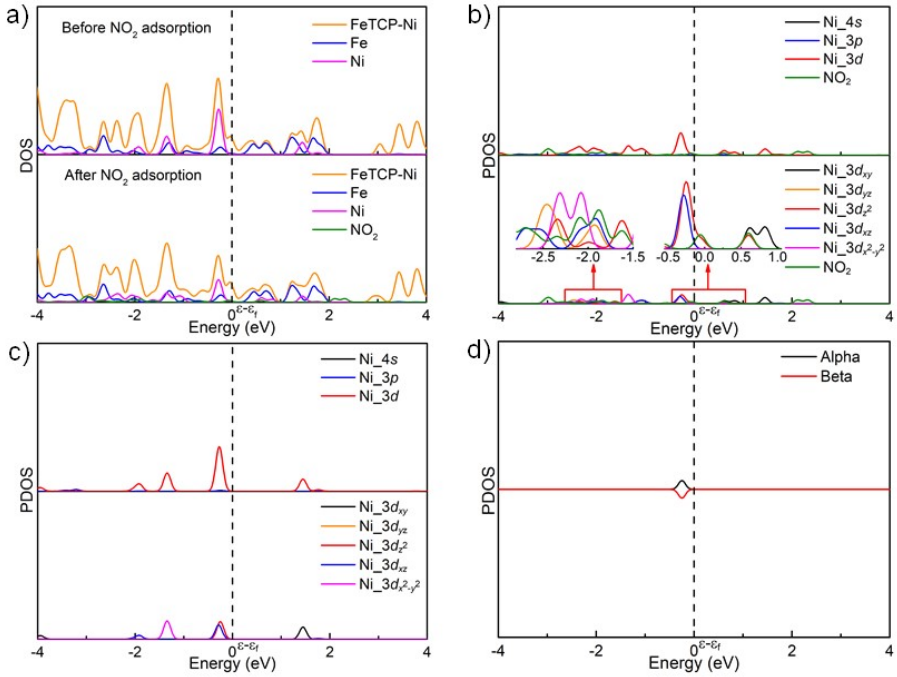

Fig. S53 (a) The TDOS and PDOS of FeTCP-Ni before and after NO_2 adsorption; (b) The PDOS of NO_2 and Ni-4*s*, Ni-3*p*, Ni-3*d* orbitals of FeTCP-Ni after NO_2 adsorption; (c) The PDOS of Ni-4*s*, Ni-3*p* and Ni-3*d* orbitals of FeTCP-Ni before NO_2 adsorption; (d) The PDOS of electron spin states in Ni-3d_z^2 orbital of FeTCP-Ni.

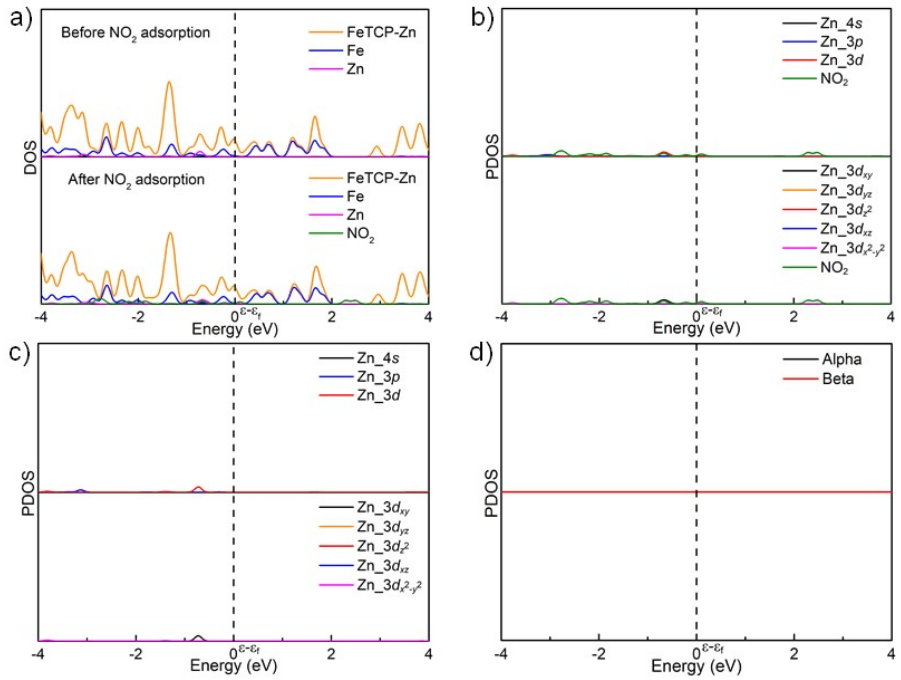

Fig. S54 (a) The TDOS and PDOS of FeTCP-Zn before and after NO_2 adsorption; (b) The PDOS of NO_2 and Zn-4*s*, Zn-3*p*, Zn-3*d* orbitals of FeTCP-Zn after NO_2 adsorption; (c) The PDOS of Zn-4*s*, Zn-3*p* and Zn-3*d* orbitals of FeTCP-Zn before NO_2 adsorption; (d) The PDOS of electron spin states in Zn-3d_z^2 orbital of FeTCP-Zn.

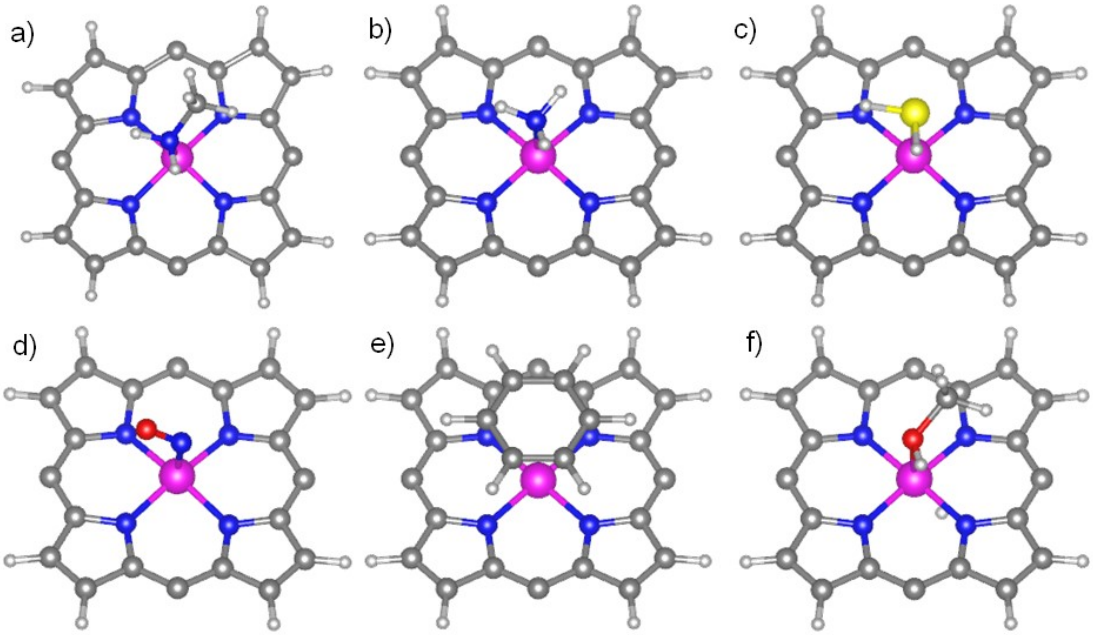

Fig. S55 The optimal adsorption configurations of different analytes on InTCP-Co, (a) CH_3NH_2; (b) NH_3; (c) H_2S; (d) NO; (e) C_6H_6; (f) CH_3OH; The other parts in the structure of InTCP-Co have been omitted for clarity in the (a)~(f).

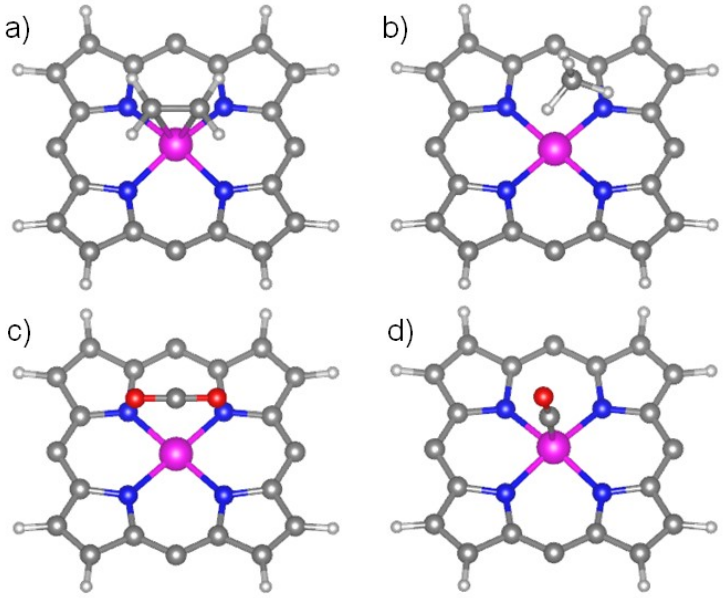

Fig. S56 The optimal adsorption configurations of different analytes on InTCP-Co, (a) CH_2CH_2; (b) CH_4; (c) CO_2; (d) CO; The other parts in the structure of InTCP-Co have been omitted for clarity in the (a)~(d).

Table S4. The adsorption energy (E_{ads}) of the different gas molecular on the InTCP-Co and the nearest atomic distance between the gas molecule and Co in InTCP-Co

	E_{ads} (eV)	*d* (Co-X, Å)
NO_2	-3.08	1.877
CH_3NH_2	-2.41	1.954
NH_3	-0.96	2.024
H_2S	-0.69	2.269
NO	-1.88	1.801
C_6H_6	-0.74*	3.297
CH_3OH	-0.70	2.218
C_2H_4	-0.72	2.184
CH_4	-0.31	2.652
CO_2	-0.30	3.209
CO	-1.18	1.755

*The adsorption energy between C_6H_6 and InTCP-Co may cause by the π-π interaction between benzene ring and porphyrin ring.

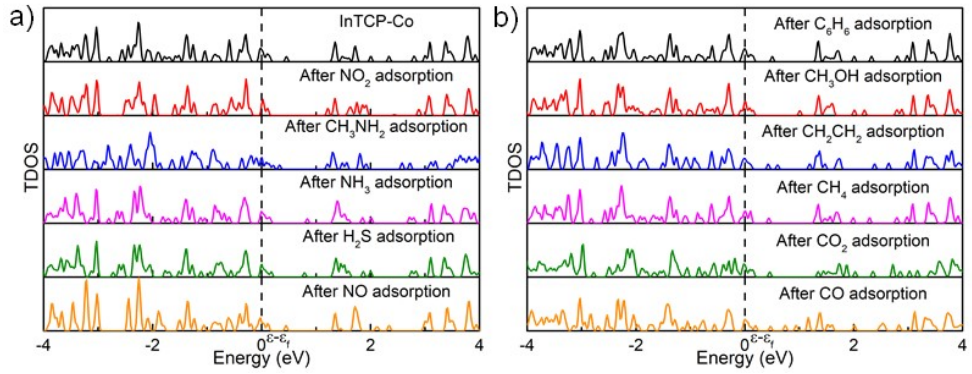

Fig. S57 The TDOS of InTCP-Co before and after different analytes adsorption.

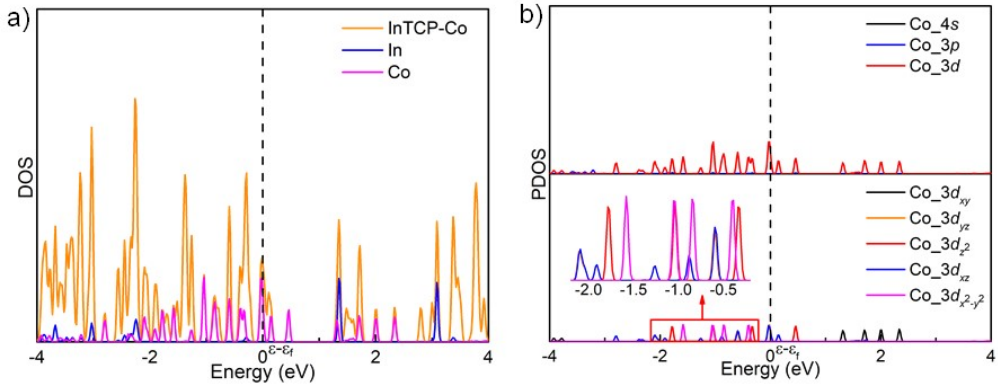

Fig. S58 (a) The TDOS and PDOS of InTCP-Co before analytes adsorption; (b) The PDOS of Co-4*s*, Co-3*p*, Co-3*d* orbitals of InTCP-Co before analytes adsorption.

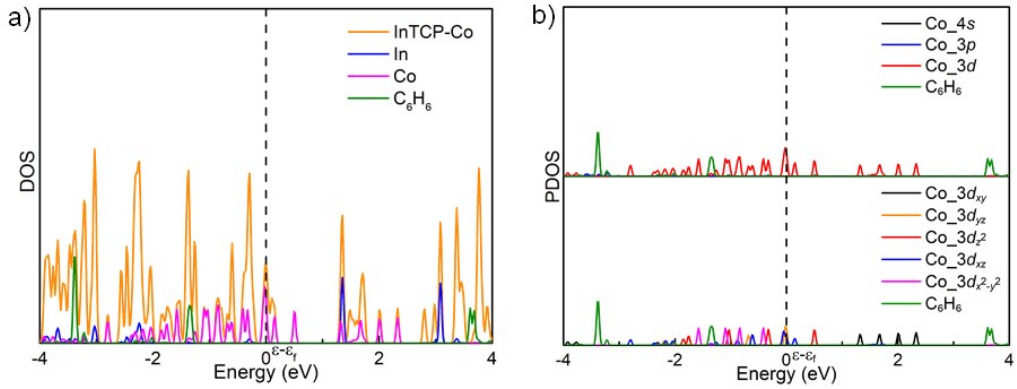

Fig. S59 (a) The TDOS and PDOS of InTCP-Co after C_6H_6 adsorption; (b) The PDOS of C_6H_6 and Co-4*s*, Co-3*p*, Co-3*d* orbitals of InTCP-Co after C_6H_6 adsorption.

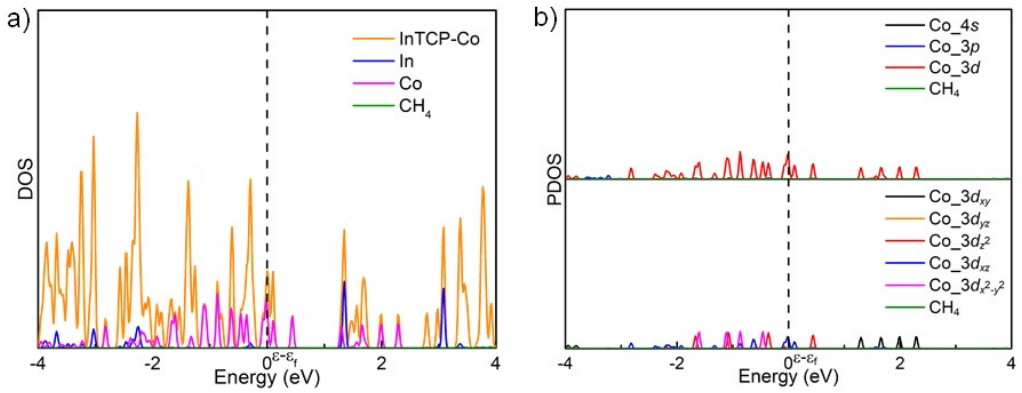

Fig. S60 (a) The TDOS and PDOS of InTCP-Co after CH_4 adsorption; (b) The PDOS of CH_4 and Co-4*s*, Co-3*p*, Co-3*d* orbitals of InTCP-Co after CH_4 adsorption.

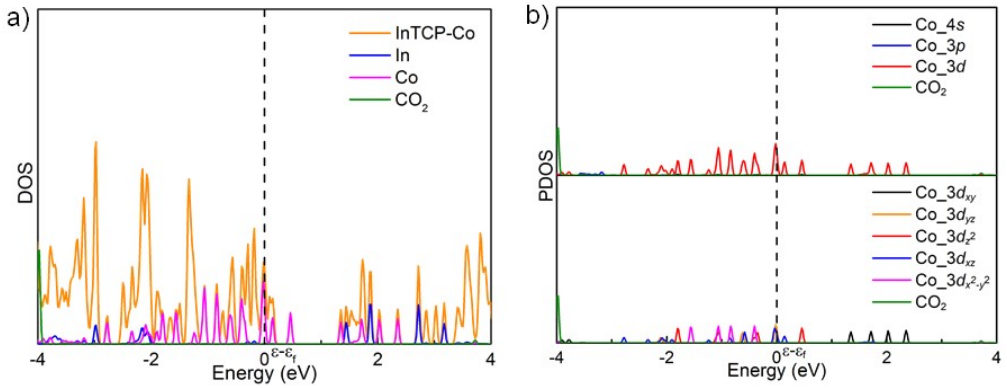

Fig. S61 (a) The TDOS and PDOS of InTCP-Co after CO_2 adsorption; (b) The PDOS of CO_2 and Co-4*s*, Co-3*p*, Co-3*d* orbitals of InTCP-Co after CO_2 adsorption.

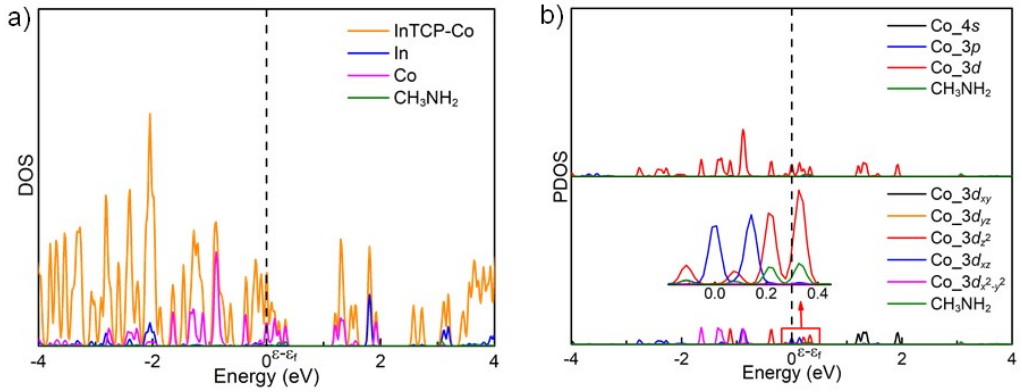

Fig. S62 (a) The TDOS and PDOS of InTCP-Co after CH_3NH_2 adsorption; (b) The PDOS of CH_3NH_2 and Co-4*s*, Co-3*p*, Co-3*d* orbitals of InTCP-Co after CH_3NH_2 adsorption.

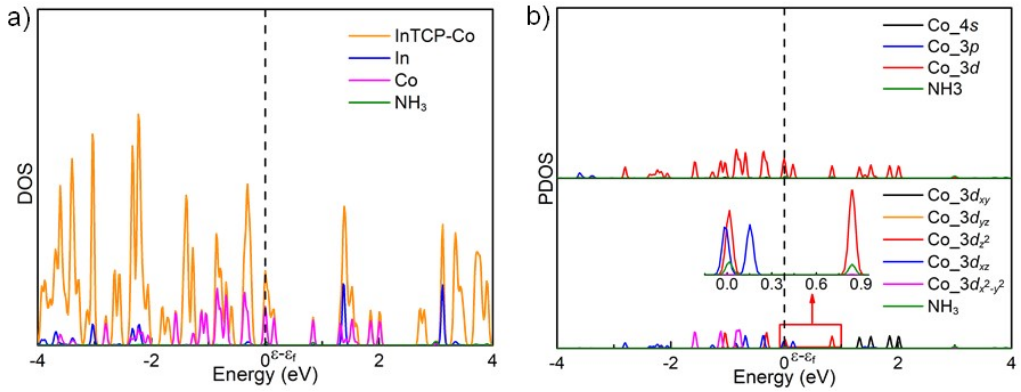

Fig. S63 (a) The TDOS and PDOS of InTCP-Co after NH_3 adsorption; (b) The PDOS of NH_3 and Co-4*s*, Co-3*p*, Co-3*d* orbitals of InTCP-Co after NH_3 adsorption.

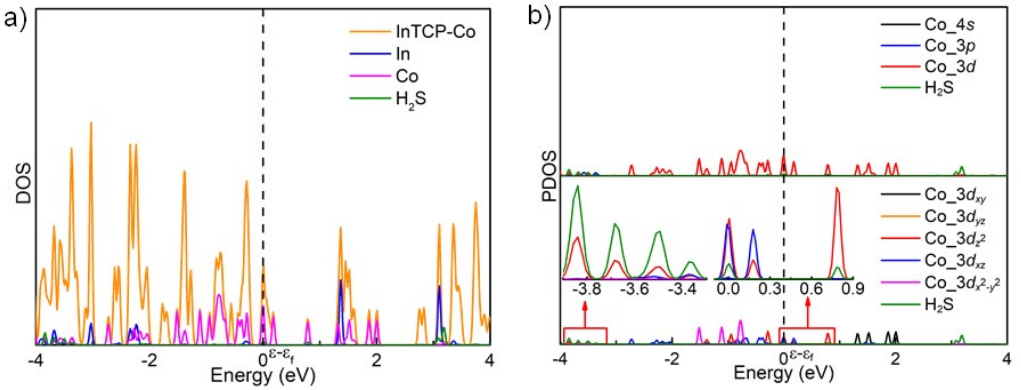

Fig. S64 (a) The TDOS and PDOS of InTCP-Co after H_2S adsorption; (b) The PDOS of H_2S and Co-4*s*, Co-3*p*, Co-3*d* orbitals of InTCP-Co after H_2S adsorption.

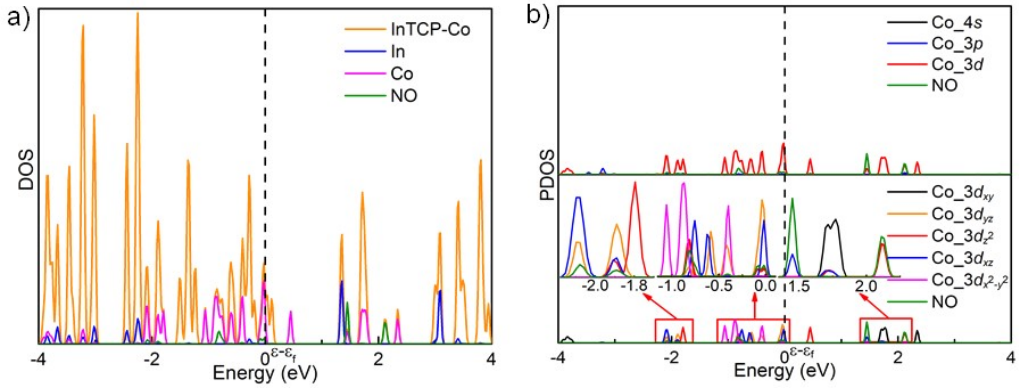

Fig. S65 (a) The TDOS and PDOS of InTCP-Co after NO adsorption; (b) The PDOS of NO and Co-4*s*, Co-3*p*, Co-3*d* orbitals of InTCP-Co after NO adsorption.

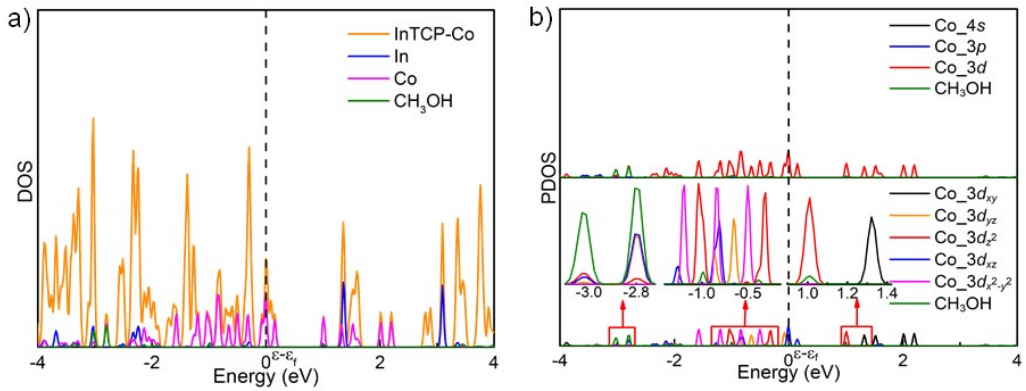

Fig. S66 (a) The TDOS and PDOS of InTCP-Co after CH_3OH adsorption; (b) The PDOS of CH_3OH and Co-4*s*, Co-3*p*, Co-3*d* orbitals of InTCP-Co after CH_3OH adsorption.

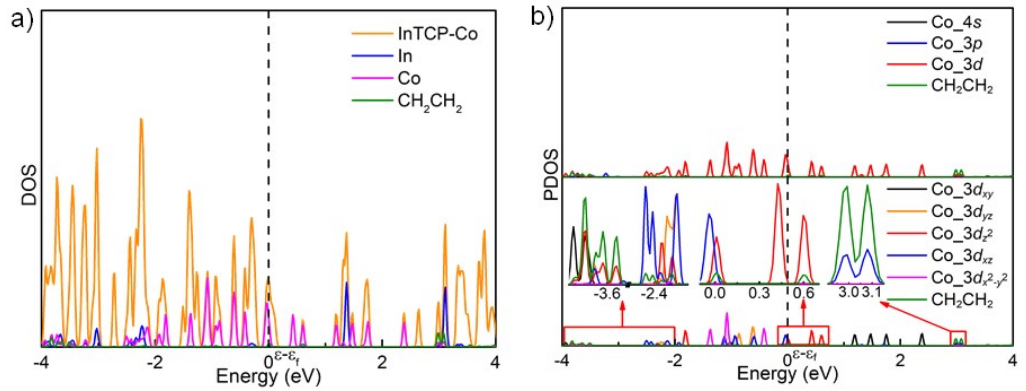

Fig. S67 (a) The TDOS and PDOS of InTCP-Co after CH_2CH_2 adsorption; (b) The PDOS of CH_2CH_2 and Co-4*s*, Co-3*p*, Co-3*d* orbitals of InTCP-Co after CH_2CH_2 adsorption.

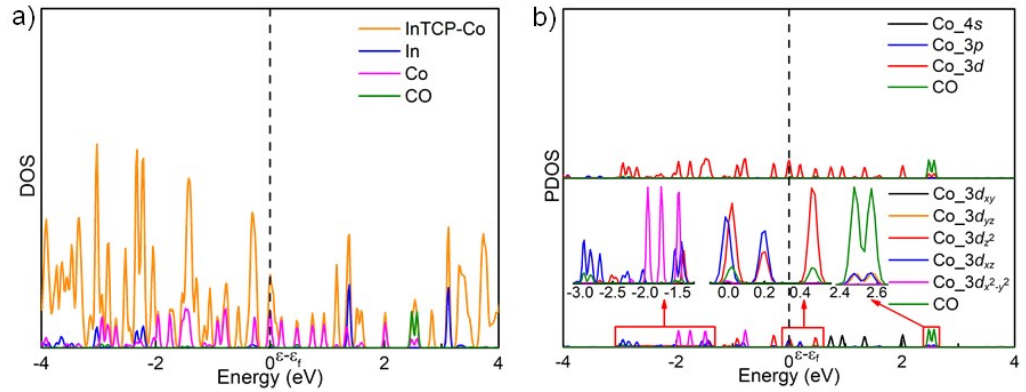

Fig. S68 (a) The TDOS and PDOS of InTCP-Co after CO adsorption; (b) The PDOS of CO and Co-4*s*, Co-3*p*, Co-3*d* orbitals of InTCP-Co after CO adsorption.

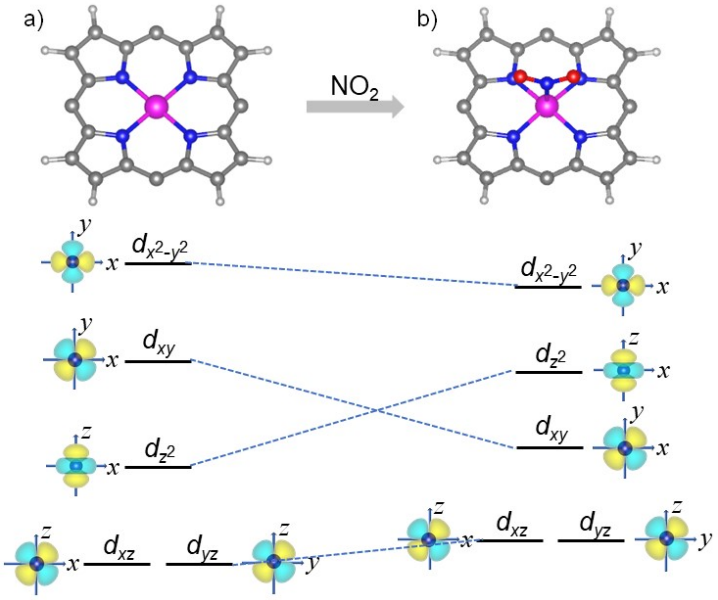

Fig. S69. (a) The coordination configuration of Co before InTCP-Co adsorbed NO_2 and the *d* orbitals energy level splitting of Co; (b) The coordination configuration of Co after InTCP-Co adsorbed NO_2 and the *d* orbitals energy level splitting of Co.

Section 11 References

1. E.-X. Chen, M. Qiu, Y.-F. Zhang, L. He, Y.-Y. Sun, H.-L. Zheng, X. Wu, J. Zhang and Q. Lin, *Angew. Chem. Int. Ed.*, 2022, **61**, e202111622.
2. E.-X. Chen, M. Qiu, Y.-F. Zhang, Y.-S. Zhu, L.-Y. Liu, Y.-Y. Sun, X. Bu, J. Zhang and Q. Lin, *Adv. Mater.*, 2018, **30**, 1704388.
3. W. J. Albery, P. N. Bartlett, C. C. Jones and L. R. Milgrom, *J. Chem. Research (s)*, 1985, 364-365.
4. Y. J. Chen, M. Liu, J. Chen, X. Huang, Q. H. Li, X. L. Ye, G. E. Wang and G. Xu, *Chem. Sci.*, 2023, **14**, 4824-4831.
5. H.-Z. Li, Y. Pan, Q. Li, Q. Lin, D. Lin, F. Wang, G. Xu and J. Zhang, *J. Mater. Chem. A*, 2023, **11**, 965-971.
6. W.-H. Deng, L. He, E.-X. Chen, G.-E. Wang, X.-L. Ye, Z.-H. Fu, Q. Lin and G. Xu, *J. Mater. Chem. A*, 2022, **10**, 12977-12983.
7. Y. Liu, X. Li, X. Li, C. Shao, C. Han, J. Xin, D. Lu, L. Niu, Y. Tang and Y. Liu, *Sens. Actuators B Chem.*, 2022, **365**, 131926.
8. C. Zhang, A. Boudiba, P. De Marco, R. Snyders, M.-G. Olivier and M. Debliquy, *Sens. Actuators B Chem.*, 2013, **181**, 395-401.
9. C. Zhang, J. Wang, M.-G. Olivier and M. Debliquy, *Sens. Actuators B Chem.*, 2015, **209**, 69-77.
10. T. Wang, Q. Yu, S. Zhang, X. Kou, P. Sun and G. Lu, *Nanoscale*, 2018, **10**, 4841-4851.
11. X. Geng, D. Lahem, C. Zhang, C.-J. Li, M.-G. Olivier and M. Debliquy, *Ceram. Int.*, 2019, **45**, 4253-4261.
12. X. Geng, P. Lu, C. Zhang, D. Lahem, M.-G. Olivier and M. Debliquy, *Sens. Actuators B Chem.*, 2019, **282**, 690-702.
13. X. Tian, X. Yang, F. Yang and T. Qi, *Colloid. Surface. A*, 2019, **578**, 123621.
14. N. M. Hung, N. M. Hieu, N. D. Chinh, T. T. Hien, N. D. Quang, S. Majumder, G. Choi,

C. Kim and D. Kim, *Sens. Actuators B Chem.*, 2020, **313**, 128001.
15. D. Liu, Z. Tang and Z. Zhang, *Sens. Actuators B Chem.*, 2020, **324**, 128754.
16. H. Wang, J. Bai, M. Dai, K. Liu, Y. Liu, L. Zhou, F. Liu, F. Liu, Y. Gao, X. Yan and L. Geyu, *Sens. Actuators B Chem.*, 2020, **304**, 127287.
17. J. Wang, C. Hu, Y. Xia and S. Komarneni, *Ceram. Int.*, 2020, **46**, 8462-8468.
18. X.-X. Wang, H.-Y. Li and X. Guo, *J. Mater. Chem. A*, 2020, **8**, 14482-14490.
19. J. Zeng, Y. Niu, Y. Gong, Q. Wang, H. Li, A. Umar, N. F. de Rooij, G. Zhou and Y. Wang, *ACS Sens.*, 2020, **5**, 3172-3181.
20. T. H. Eom, S. H. Cho, J. M. Suh, T. Kim, T. H. Lee, S. E. Jun, J. W. Yang, J. Lee, S.-H. Hong and H. W. Jang, *J. Mater. Chem. A*, 2021, **9**, 11168-11178.
21. C. Han, X. Li, Y. Liu, Y. Tang, M. Liu, X. Li, C. Shao, J. Ma and Y. Liu, *Adv. Sci.*, 2021, **8**, e2102471.
22. Y. M. Jo, K. Lim, J. W. Yoon, Y. K. Jo, Y. K. Moon, H. W. Jang and J. H. Lee, *ACS. Cent. Sci.*, 2021, **7**, 1176-1182.
23. K. Lim, Y. M. Jo, J. W. Yoon, J. S. Kim, D. J. Lee, Y. K. Moon, J. W. Yoon, J. H. Kim, H. J. Choi and J. H. Lee, *Small*, 2021, **17**, e2100438.
24. Y. Xia, S. He, J. Wang, L. Zhou, J. Wang and S. Komarneni, *Chem. Commun.*, 2021, **57**, 9136-9139.
25. T. H. Eom, S. H. Cho, J. M. Suh, T. Kim, J. W. Yang, T. H. Lee, S. E. Jun, S. J. Kim, J. Lee, S. H. Hong and H. W. Jang, *Small*, 2022, **18**, e2106613.
26. Y. Sun, J. Hu and Y. Zhang, *Sens. Actuators B Chem.*, 2022, **367**, 132032.
27. T. Wang, J. Liu, Y. Zhang, Q. Liang, R. Wu, H.-S. Tsai, Y. Wang and J. Hao, *J. Mater. Chem. A*, 2022, **10**, 4306-4315.
28. S. Han, L. Li, C. Ji, X. Liu, G. E. Wang, G. Xu, Z. Sun and J. Luo, *J. Am. Chem. Soc.*, 2023, **145**, 12853-12860.